Computer Methods in Applied Mechanics and Engineering manuscript No.
(will be inserted by the editor)

A unified variational eigen-erosion framework for interacting brittle fractures and compaction bands in fluid-infiltrating porous media

Kun Wang · WaiChing Sun

Received: January 1, 2017/ Accepted: date

Abstract The onset and propagation of the cracks and compaction bands, and the interactions between them in the host matrix, are important for numerous engineering applications, such as hydraulic fracture and CO2 storage. While crack may become flow conduit that leads to leakage, formation of compaction band often accompanies significant porosity reduction that prevents fluid to flow through. The objective of this paper is to present a new unified framework that predicts both the onset, propagation and interactions among cracks and compaction bands via an eigen-deformation approach. By extending the generalized Griffith's theory, we formulate a unified nonlocal scheme that is capable to predict the fluid-driven fracture and compression-driven anti-crack growth while incorporating the cubic law to replicate the induced anisotropic permeability changes triggered by crack and anti-crack growth. A set of numerical experiments are used to demonstrate the robustness and efficiency of the proposed model.

Keywords compaction band; eigen-erosion; porous media; hydraulic fracture; anti-crack; hydraulic aperture

1 Introduction

Crack growth in fluid-infiltrating porous media has important implications on many engineering applications and activities. The onset, nucleation, branching and coalescence of cracks may dictate the success of geological disposals of carbon dioxide, hydraulic fracture operation, geothermal energy extraction, storage of nuclear waste underground and the tunneling. In the case where the void space of the porous media is filled with fluid, the propagation of fracture may also lead to significant increase in effective permeability and induced anisotropy in the hydraulic responses of the porous media [Haimson et al., 1967, Zoback et al., 1977, Detournay, 2016]. Perhaps a less well-known fact to the general public is that porous media may also form compaction band. As shown in Figure 1, a compaction band is a narrow zone in which large porosity reduction is observed in an otherwise intact host matrix [Antonellini et al., 1994, Haimson, 2001, Schultz et al., 2010, Sun et al., 2011b].

Due to the highly localized porosity reduction, pure and shear-enhanced compaction band may lead to up to several orders of permeability reduction [Baud et al., 2004, Fossen et al., 2011, Sun et al., 2011b,a, Holcomb and Olsson, 2003]. Depending on the mineralogy, porosity, grain size, loading conditions and other environmental factors, compaction band and fractures may coexist in a hydro-geological system. The interactions between them in the host matrix may profoundly alter the mechanical and hydraulic characteristics. For instance, in a series of papers (Haimson and Song [1993], Lee and Haimson [1993], Haimson [2001], Haimson and Lee [2004]), Haimson and co-workers have generated a collection of experimental evidence to support that borehole breakouts, the elongations of borehole cross-section resulting from preferential

Corresponding author: WaiChing Sun
Assistant Professor, Department of Civil Engineering and Engineering Mechanics, Columbia University , 614 SW Mudd, Mail Code: 4709, New York, NY 10027 Tel.: 212-854-3143, Fax: 212-854-6267, E-mail: wsun@columbia.edu

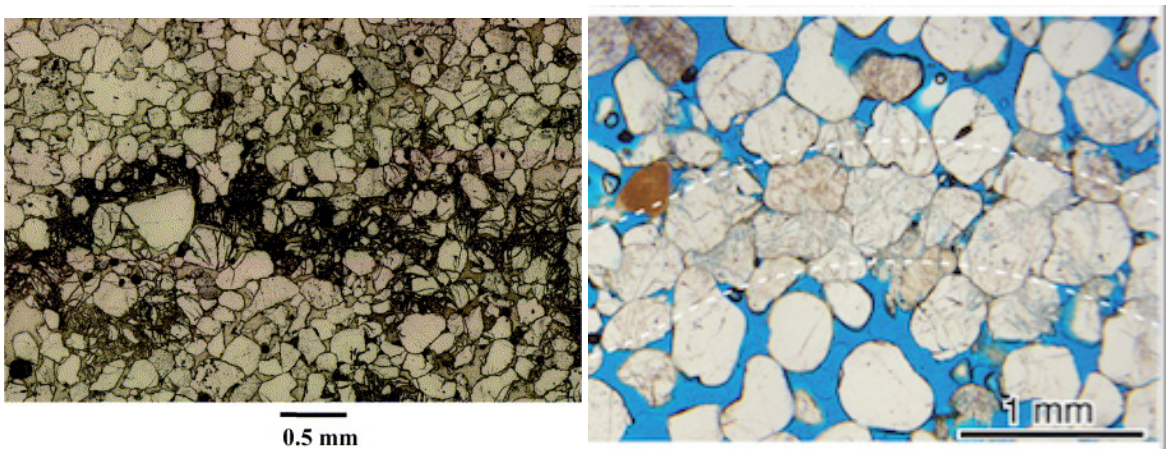

Fig. 1: (LEFT) SEM image of a laboratory-reproduced compaction band in Bentheim sandstone reported in Baud et al. [2004] (RIGHT) SEM image of a field compaction band in Navajo Sandstone found in Buckskin Gulch site, Utah as reported in Fossen et al. [2011] (Figure reproduced from Baud et al. [2004], Fossen et al. [2011]).

rock failure, is related to the propagation of both the fracture and compaction band. Their experimental data also indicate that the compaction band, which advances orthogonally to the maximum compressive stress, can be regarded as a Mode I anti-crack in the LEFM framework [Sternlof et al., 2005]. Related findings can also be found in the laboratory tests, such as Stanchits et al. [2009], Charalampidou et al. [2014], in which notched specimen are used to study the initiation and propagation of compaction band and measure the two fracture energies related respectively to fracture and compaction bands, as shown in Figure 2.

These experimental findings are further validated in the field work performed on the Aztec Sandstone found in the Valley of Fire, Nevada, in which another series of theoretical and experimental studies (e.g. Mollema and Antonellini [1996], Sternlof et al. [2005], Rudnicki and Sternlof [2005], Rudnicki [2007]), have found that the normal contractional strain across the compaction band is nearly constant, which implies that a constant driving stress along the compaction bands with negligibly small processing zone. These results are consistent with the LEFM anti-crack interpretation based on Griffith's theory. First pointed out by Sternlof et al. [2005], the anti-crack theory on compaction band explains the initiation and propagation of compaction bands as the consequence of Griffith-type grain-scale flaw collapses due to weak grains, irregular pores or other causes. This similarity with Griffith's theory on brittle fracture provides an opportunity for us to derive a unified variational framework in which the propagation of both cracks and anti-cracks are viewed as the competition between the surface energy and the restitution of bulk energy during crack or compaction band growth [Francfort and Marigo, 1998, Bourdin et al., 2008].

It should be noted that the anti-crack theory is not the only one accepted theoretical framework to interpret the onset of compaction band. In particular, bifurcation analysis has also been widely used to predict the onset of the compaction band at the continuum scale [Issen and Rudnicki, 2001, Aydin et al., 2006, Chemenda, 2011]. As pointed out in Charalampidou et al. [2014], the drawback of this approach is that it is difficult to apply bifurcation analysis to predict compaction band patterns on heterogeneous material or to explain the various geometrical features such as the wiggly patterns recently found in Liu et al. [2015].

While there are many discrete modeling approaches proposed in to simulate compaction band and fractures with either DEM or lattice-spring network (e.g. Katsman et al. [2005], Wang et al. [2008], Liu et al. [2015], Lee et al. [2016a]), the applicability of these models are limited to interpretation of micro-scale mechanism in the laboratory under full drained condition. This limitation is likely related to (1) the prohibitive computational cost to simulate grain-scale processes at the field scale, (2) the difficulty to calibrate material parameters for grain crushing and fragmentation process, and (3) the difficult to properly introduce the hydro-mechanical effect in the grain scale with a 2D DEM and lattice-spring model.

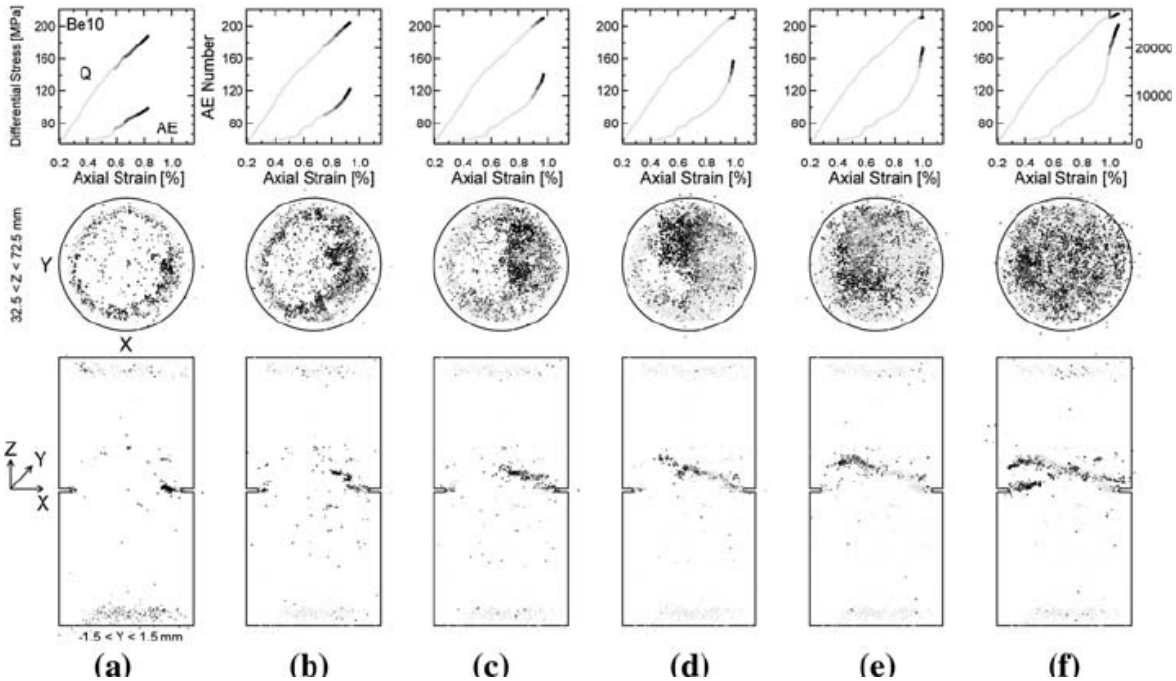

Fig. 2: Compaction band initiation and propagation in a wet Bentheim Sandstone specimen reported in Stanchits et al. [2009] (Figure reproduced from Stanchits et al. [2009]).

On the other hand, there are significant progress made in the development of numerical approaches for simulating the propagation of fluid-driven fracture at the macroscopic continuum scale. For instance, cohesive zone interface element can be inserted to model the fracture process zone when the crack path is known a priori in a finite element framework. The Poiseuille flow along the cracks is then simulated with finite element or finite difference methods to capture the hydro-mechanical coupling effect. [Boone et al., 1986, Secchi and Schrefler, 2012, Carrier and Granet, 2012]. Another popular modeling technique is to introduce enhancement basis in the finite element space to capture the crack as a strong discontinuity. The X-FEM and assumed strain model are examples where cracks are explicitly represented as a sharp interface [Armero and Callari, 1999, Gupta and Duarte, 2014, Salimzadeh and Khalili, 2015]. Nevertheless, the efficiency of the embedded strong discontinuity approach often comes with the price that one must be able to generate proper mathematical representation of the geometry and topology of the cracks. This is not a big issue if the crack is straight. However, the modeling of curved crack path, crack branching and coalescence is by no mean straightforward [Khoei, 2014]. Furthermore, in order to simulate the crack propagation via the embedded strong discontinuity approach, modelers must select among multiple criteria or models that predict the onset (c.f. [Begley and Landes, 1972]) and propagation direction (e.g. maximum hoop stress criterion), and detect potential branching [Linder and Armero, 2009] for a particular situation. This selection process can be a trial-and-error empirical task that greatly depends on independent tastes and intuition.

Fracture surface may also be approximated by a phase-field or smeared crack model where the location of the crack is represented by an implicit function but the displacement field itself may remains smooth [Bourdin et al., 2008, Amor et al., 2009, Borden et al., 2012, Miehe and Mauthe, 2016, Clayton and Knap, 2016, Lee et al., 2016b]. A notable departure of this approach from the embedded strong discontinuity approach is that one may recast it as an energy minimization problem and the onset, propagation, branching and coalescence of fractures can be simulated without introducing any additional criterion for each mechanism. Nevertheless, recent work, particularly, Farrell and Maurini [2016] has shown that the phase-field model can be computationally demanding due to the imposed demands to resolve the small length scales. The popular operator-split algorithm is robust, but convergence can be slow due to the large,

ill-conditioned linear sub-problems that sequentially updates the phase field and displacement. Another approach that does not introduce shape interface is the element erosion method in which element is simply deleted when a specific criterion is met. This method is understandably very easy to implement, but also exhibits severe mesh dependence. This problem is recently cured in Schmidt et al. [2009] where a variational framework similar to Bourdin et al. [2008] is incorporated into the Griffith's fracture theory. This approach interprets the deformation in the eroded element as an eigen-deformation while introducing a nonlocal regularized fracture energy to eliminate the mesh dependence. Pandolfi and Ortiz [2012] develops a simple finite element erosion method based on this eigen-fracture scheme. Like the phase field approach, the eigen-fracture model is capable of capturing curved crack path, crack branching and coalescence without the spurious mesh dependency. However, there is no additional field variable introduced in the numerical model and hence relatively easy to implement. Nevertheless, the extension to poromechanics problem has not yet been considered.

Due to the wide spectrum of engineering applications related to fractures and compaction bands, a unified numerical model that can both predict the onset, propagation, branching and coalescence of compaction band and fractures and the interaction between them in fluid-infiltrating porous media is invaluable. While there are numerous efforts to separately model fractures and compaction band at the continuum scale, to the best of the authors' knowledge, there has not yet any attempt to propose numerical model that can capture both the fracture and compaction band in fluid-infiltrating porous media within a unified Griffith fracture framework.

The objective of this research is to present a consistent and unified theory and develop a feasible numerical approach to fulfill this knowledge gap. In particular, we introduce a generalization of the eigen-deformation and corresponding dissipation energy such that fracture and compaction band can be idealized as cracks and mode I anti-crack. Due to the existence of two dissipation mechanisms, we use the spectral decomposition to split the stored elastic energy into the tensile and compressive parts such that the onset of different eigen-deformation within each element is driven by the corresponding types of regularized dissipation energy. Given the fact that hydraulic aperture is rarely identical to the mechanical aperture, we introduce a path-searching algorithm to introduce a nonlocal cubic law in the eigen-erosion element. This introduction of regularization is found to be essential to ensure that the enhancement or suppression of hydraulic energy dissipation due to the formation of shear band and compaction band in the eroded elements converges upon mesh refinement. Consequently, the proposed model allows one to simulate the onset, propagation and coalescence of both fractures and compaction band, all within a consistent variational framework. This is done without introducing additional criteria to determine fracture propagation direction, without the need of inserting additional degree of freedom during the simulations to reflect the altering geometry of the cracks, and without the introduction of any nodal solution in the discretized finite element model. The simplicity achieved in this work is important to ensure the proposed method feasible to practicing engineers and scientists.

The rest of this paper is organized as follows. We first explain the modeling of the onset and propagation of fractures and compaction bands in fluid-infiltrating porous media within a variational framework (Section 2). We then highlight the important aspects of the numerical implementation, such as the split of tensile and compressive strain, and the introduction of the regularized cubic law specific for the eigen-fracture problems (Section 3). Numerical examples are used to demonstrate the hydromechanical interactions among the propagating fractures and compaction bands (Section 4). A conclusion that summarizes the major points of this work is introduced in the Section 5.

As for notations and symbols, bold-faced letters denote tensors; the symbol '$\cdot$' denotes a single contraction of adjacent indices of two tensors (e.g. $\boldsymbol{a} \cdot \boldsymbol{b} = a_i b_i$ or $\boldsymbol{c} \cdot \boldsymbol{d} = c_{ij} d_{jk}$); the symbol ':' denotes a double contraction of adjacent indices of tensor of rank two or higher (e.g. $\boldsymbol{C} : \boldsymbol{\epsilon}^{\boldsymbol{e}} = C_{ijkl} \epsilon^e_{kl}$); the symbol '$\otimes$' denotes a juxtaposition of two vectors (e.g. $\boldsymbol{a} \otimes \boldsymbol{b} = a_i b_j$) or two symmetric second order tensors (e.g. $(\boldsymbol{\alpha} \otimes \boldsymbol{\beta}) = \alpha_{ij} \beta_{kl}$). As for sign conventions, unless specify otherwise, we consider the direction of the tensile stress and dilative pressure as positive.

2 Multiphysical eigen-fracture model for hydro-mechanical problems

We present a unified framework that predicts the growth of both cracks and anti-cracks in brittle fluid-saturated porous media using the eigen-erosion approach. The relation between eigen-fracture model and generalized Griffith's theory for brittle fracture is first examined in Schmidt et al. [2009], and subsequently further developed in Pandolfi and Ortiz [2012] to simulate crack growth in a finite element framework. This fracture model contains an energy functional depending on the displacement field $\boldsymbol{u}$, a field of eigen-deformation $\boldsymbol{\varepsilon}^*$ and a small regularization parameter ϵ. $\boldsymbol{\varepsilon}^*$ allows the displacement field to exhibit discontinuity with no cost of local elastic energy, thus can describe the fracture occurred in the body. The derived eigen-erosion scheme, which is a mesh independent element deletion approach, restricts the eigen-deformation to be either $\mathbf{0}$ in the intact linear elastic elements, or equal to the local strain $\boldsymbol{\varepsilon}(\boldsymbol{u}) = \frac{1}{2}(\nabla\boldsymbol{u} + \nabla\boldsymbol{u}^{\mathrm{T}})$ in elements representing the crack. Here our new contribution is to extend this framework to include eigen-deformation that represent not only fracture but also *anti-crack*. We also include additional terms in the energy functional to account for pore fluid contribution.

In fluid-saturated porous media, the external loading imposed on porous solid is partially carried by the solid skeleton and partially supported by the fluid [Terzaghi, 1936, Biot, 1941]. Following the effective stress principle, the total stress $\boldsymbol{\sigma}$ is decomposed to the effective stress $\boldsymbol{\sigma}'$ acting on grains and a hydrostatic stress:

$$\boldsymbol{\sigma} = \boldsymbol{\sigma}' - bp^f\boldsymbol{I}\ ;\ b = 1 - \frac{K}{K_s}, \tag{1}$$

where p^f is the pore fluid pressure, b is the Biot's coefficient, $\boldsymbol{I}$ is the identity tensor, K and K_s are the bulk modulus of the solid skeleton and that of the solid grains. The effective stress principle motivates the decomposition of total elastic energy into effective strain energy stored in solid skeleton and energy stored in pore fluid [Armero and Callari, 1999], i.e.,

$$W(\boldsymbol{\varepsilon}, \boldsymbol{\varepsilon}^*, p^f) = W_{\mathrm{eff}}(\boldsymbol{\varepsilon}, \boldsymbol{\varepsilon}^*) + W_{\mathrm{fluid}}(\boldsymbol{\varepsilon}, p^f). \tag{2}$$

For linear elastic solid skeleton, the effective strain energy takes the form:

$$W_{\mathrm{eff}}(\boldsymbol{\varepsilon}, \boldsymbol{\varepsilon}^*) = \int_\Omega \frac{1}{2}(\boldsymbol{\varepsilon} - \boldsymbol{\varepsilon}^*) : \boldsymbol{\mathcal{C}}^e : (\boldsymbol{\varepsilon} - \boldsymbol{\varepsilon}^*)dV \tag{3}$$

where Ω is the domain of the elastic body, $\mathcal{C}^e$ is the forth-order elasticity tensor of the solid skeleton. The eigen-deformation field takes different values in intact solid, crack C and compaction band CB:

$$\boldsymbol{\varepsilon}^*(\boldsymbol{x}, t) = \begin{cases} \boldsymbol{\varepsilon}^+(\boldsymbol{x}, t) & \boldsymbol{x} \in C \\ \varepsilon_{\mathrm{inel}}\boldsymbol{n}_{CB}(\boldsymbol{x}, t) \otimes \boldsymbol{n}_{CB}(\boldsymbol{x}, t) & \boldsymbol{x} \in CB \\ \mathbf{0} & \boldsymbol{x} \in \Omega \setminus (C \cup CB) \end{cases} \tag{4}$$

This choice of eigen-deformation field implies that we assume the zero-traction boundary conditions across the crack, which is suitable for brittle fracture. As for the compaction band, the assumption is made based on experimental observations: upon compaction band formation, the grain crushing and pore collapse induce significant uniaxial inelastic strain $\varepsilon_{\mathrm{inel}}$ (e.g., 10%) along the principal direction of maximum compressive stress $\boldsymbol{n}_{CB}$ [Sternlof et al., 2005]. The numerical value of $\varepsilon_{\mathrm{inel}}$ is a material parameter calibrated to match the experimental porosity reduction (private communication, Rudnicki, 2016). Another underlying simplification is that the elastic property of the compaction band does not differ significantly from the host matrix. The latter simplification is likely to be feasible for limited cases only and should be considered with caution. For instance, in the natural compaction bands found in the Aztec Sandstone formation, the compaction band is stiffer than the host rock due to the local pressure solution healing, porosity loss and effective grain size distribution. Meanwhile, the shear modulus is affected by competing mechanisms, i.e., the reduced porosity, which enhances shear stiffness, and the micro-fracturing and effective grain size reduction which reduce shear stiffness [Sternlof et al., 2005]. On the other hand, the effect of elastic modulus difference between the host matrix and the compaction band has been studied in Rudnicki and Sternlof [2005] and Rudnicki [2007], where the strain energy per unit area required to propagate the compaction band in an infinite layer of finite thickness corresponding for compaction band of different stiffness are analyzed. The analyses concluded that the mismatch of elastic moduli has a relatively small effect on the stress

ahead of the band and the energy release comparing to that of the far-field stress and the amount of inelastic compactive strain triggered by the compaction band. Nevertheless, a more refined phenomenological or micro-structure based model that can more accurately captures the evolving relationship between the elastic behaviors of the compaction band and the host rock may still bring new insights into the interpretation of critical energy release rate and the influences of microstructural attributes on the constitutive responses of compaction bands. Such an improvement remains a significant challenge due to the difficulties to generating reliable measurements of the very thin and tabular compaction bands in the laboratories (e.g. Sternlof et al. [2005]) and will only be considered in the future when the relevant data becomes available.

In this study, a material element is allowed to be simultaneously in crack set C and compaction band CB in the proposed model, i.e., $C \cap CB \neq \emptyset$. A compaction band zone could become crack, as observed in borehole breakout experiments that anti-dilatant failure zone presents at the tip of fracture-like breakout in sandstone with high porosity [Haimson, 2001]. On the other hand, once a material element is cracked, it is excluded from the compaction band detection scheme to enforce the appropriate path-dependent behaviors.

The fluid contribution to the total elastic energy reads [Armero and Callari, 1999, Miehe and Mauthe, 2016]:

$$W_{\text{fluid}}(\boldsymbol{\varepsilon}, p^f) = \frac{M}{2}[(1-b)\varepsilon_v - \frac{p^f}{M}]^2 \tag{5}$$

where $\varepsilon_v = \text{trace}(\boldsymbol{\varepsilon})$ is the volumetric strain, M is the Biot's modulus defined as [Nur and Byerlee, 1971]:

$$M = \frac{K_s K_f}{K_f(b-\phi) + K_s \phi} \tag{6}$$

with ϕ being the porosity, K_s and K_f being the bulk modulus of solid particle and pore fluid, respectively. The dissipation associated with the Darcian flow of the pore fluid $\mathcal{D}_f(\boldsymbol{\varepsilon}, \boldsymbol{\varepsilon}^*, p^f)$ is expressed as:

$$\mathcal{D}_f(\boldsymbol{\varepsilon}, \boldsymbol{\varepsilon}^*, p^f) = -\int_0^t [\int_\Omega \frac{1}{2} \frac{\boldsymbol{\kappa}(\boldsymbol{\varepsilon}, \boldsymbol{\varepsilon}^*)}{\mu} : (\nabla p^f \otimes \nabla p^f) dV] d\tau \tag{7}$$

where μ is the dynamic viscosity of fluid and $\boldsymbol{\kappa}(\boldsymbol{\varepsilon}, \boldsymbol{\varepsilon}^*)$ is the effective permeability of the porous medium, which we assume to be symmetric. To capture the porosity-permeability relation responsible for the formation of flow barriers (due to the compaction band formation) and flow conduits (due to to crack growth), the effective permeability is written in terms of both the deformation and the eigen-deformation of the solid skeleton. The fracture energy accounting for crack and anti-cracks, in the context of eigen-fracture, reads:

$$G_C \frac{|C_{\epsilon_C}|}{2\epsilon_C} + G_{CB} \frac{|C_{\epsilon_{CB}}|}{2\epsilon_{CB}},$$

where ϵ_C and ϵ_{CB} are length scale parameters related to crack and anti-crack, respectively. Their values can be different. The symbol $|C_\epsilon|$ denotes the "ϵ-neighborhood" of crack C or anti-crack CB, i.e., the sets of points having distance less or equal to ϵ from C or CB [Schmidt et al., 2009, Pandolfi and Ortiz, 2012]. G_C and G_{CB} are critical energy release rates. The regularized energy-dissipation functional in the context of fluid-saturated brittle porous media writes:

$$\begin{aligned} F_{(\epsilon_C, \epsilon_{CB})}(\boldsymbol{\varepsilon}, \boldsymbol{\varepsilon}^*, p^f, t) = & \int_\Omega \frac{1}{2}(\boldsymbol{\varepsilon} - \boldsymbol{\varepsilon}^*) : \boldsymbol{\mathcal{C}}^e : (\boldsymbol{\varepsilon} - \boldsymbol{\varepsilon}^*) dV - \int_{\Gamma_t} \bar{\boldsymbol{T}} \cdot \boldsymbol{u} dS \\ & + \int_\Omega \frac{M}{2}[(1-b)\varepsilon_v - \frac{p^f}{M}]^2 dV + \int_0^t [\int_\Omega \bar{s} p^f dV - \int_{\Gamma_q} \bar{\boldsymbol{q}} \cdot p^f \boldsymbol{dS}] d\tau \\ & + G_C \frac{|C_{\epsilon_C}|}{2\epsilon_C} + G_{CB} \frac{|C_{\epsilon_{CB}}|}{2\epsilon_{CB}} + \mathcal{D}_f(\boldsymbol{\varepsilon}, \boldsymbol{\varepsilon}^*, p^f). \end{aligned} \tag{8}$$

where Γ_t is the boundary on which the traction $\bar{\boldsymbol{T}}$ is applied, Γ_q is the boundary on which the flux $\bar{\boldsymbol{q}}$ is prescribed, and $\bar{s}$ is the source flux.

The regularized crack/anti-crack tracking problem consists of minimizing the above energy-dissipation functional at every time step subject to monotonicity constraint:

$$\begin{cases} C(t) \subset C(t+\Delta t) \\ CB(t) \subset CB(t+\Delta t) \end{cases}. \tag{9}$$

The finite element implementation of the eigen-fracture framework consists of taking the eigen-deformation field to be constant over one element and restricting the value in a binary case: the element is either intact (linear elastic) or completely failed (eroded). This leads to a simple element deletion approach. However, it is superior to other element erosion methods that it converges to the Griffith fracture with infinitesimal mesh size and does not exhibit spurious mesh dependencies.

The eigen-erosion approach is simple and could be easily implemented to finite element codes for continuum mechanics without intruding the existing structure, unlike some numerical schemes such as X-FEM which must insert new degrees of freedom into the global equilibrium equations. The Ids of eroded elements at time t_n are contained in the crack set C_n. The equilibrium displacement field with crack C_n is solved by conventional FEM. Then the crack-tracking scheme iterates over all elements K and computes the associated elastic energy release of the solid skeleton $-\Delta E_K$ by the explicit first-order estimation (cf. Pandolfi and Ortiz [2012]):

$$-\Delta E_K \sim \frac{1}{2}\boldsymbol{u_K}^T \cdot \boldsymbol{\Delta S_K} \cdot \boldsymbol{u_K}, \tag{10}$$

where $\boldsymbol{u_K}$ is the displacement vector of element K and $\boldsymbol{\Delta S_K}$ is its element stiffness matrix. The effective crack increment ΔA_K is also computed assuming that K is included in the new crack set C_{n+1}. The increment is defined as the area difference (in 2D problems) between the ϵ-neighborhood of crack $C_n \cup K$ and that of crack C_n. The regularization parameter ϵ defining the region supporting the computation of fracture energy is chosen to be proportional to the element size h and tends to zero more slowly than h: $\epsilon = 4h$. The net energy gain $-\Delta F_K = -\Delta E_K - G_c \Delta A_K$ is computed for each element K and the element having the largest positive energy gain is eroded from the simulation. This procedure is repeated within the time step until $-\Delta F_K$ for all elements are inferior to zero.

In the new unified eigen-erosion framework, we highlight our contribution of introducing the eigen-decomposition algorithm for crack/anti-crack tracking. This scheme is more appropriate when shear and compaction band are modeled, since it identifies the principal directions of deformation and distinguishes the tensile/compressive contributions. Another important aspect is the development of hydraulic aperture algorithm for fracture in porous media. Both scheme are detailed in the section of numerical implementation.

3 Numerical implementation

Within each time step $t \in [t_n, t_{n+1}]$, the hydro-mechanical field variables (displacement field $\boldsymbol{u}$, pore pressure field p^f) and the element-wise constant eigen-deformation field representing cracks and compaction bands are solved in a staggered manner. Given the crack and compaction band configuration obtained from the previous time step, $\boldsymbol{u}$ and p^f are updated to achieve equilibrium in response to new mechanical loading or injection of fluid. This step consists of solving the governing equations of saturated porous media (unbroken and fractured), i.e., balance of linear momentum and balance of fluid mass. The standard finite element procedure is presented in Appendix for completeness. Holding the hydro-mechanical field constant, a unified spectral-decomposition crack/anti-crack tracking scheme is then performed to update the sets of discontinuities C and CB. If new crack or anti-crack elements are identified, the hydraulic permeability matrices are updated to account for the flow conduit and flow barrier effect of crack and compaction band, respectively. A new algorithm based on a projected eigen-erosion field is proposed for determination of flow direction and hydraulic aperture inside crack. This staggered procedure is iterated until no element is added to the crack nor anti-crack sets. Algorithm 1 summarizes this unified eigen-erosion framework and important algorithmic aspects are elaborated in the following subsections. Note that other choices of solution sequence are also possible. For instance, instead of simultaneous tracking cracks and compaction bands, crack set could be updated first and the hydro-mechanical field is equilibrated before searching for new anti-crack set. In principle, the theories and algorithms presented in this work should be valid for

one-, two- and three-dimensional problems. Nevertheless, the three-dimensional simulations would only be practical if the solver is sufficiently fast to handle the fine mesh required to capture the crack paths in many 3D applications with complex fracture patterns. This extension will be considered in the future but is out of scope of this work.

Algorithm 1 Main

Require: Displacement field $\boldsymbol{u}_n$ and pore pressure field p_n^f at time t_n.
Require: Crack set C_n and anti-crack set CB_n at time t_n.
1: Set time to t_{n+1}, apply loading, initialize new crack set $C_{n+1}^0 = C_n$, new anti-crack set $CB_{n+1}^0 = CB_n$, $i = 0$.
2: Compute equilibrium displacement $\boldsymbol{u}_{n+1}^i$ and pore pressure field ${p^f}_{n+1}^i$ with C_{n+1}^i and CB_{n+1}^i.
3: Update C_{n+1}^{i+1} and CB_{n+1}^{i+1} (Algorithm 2).
4: Update local permeability of C_{n+1}^{i+1} and CB_{n+1}^{i+1} (Algorithm 3 or 4).
5: **if** $C_{n+1}^{i+1} \neq C_{n+1}^i$ or $CB_{n+1}^{i+1} \neq CB_{n+1}^i$ **then**
6: $\quad i \leftarrow i + 1$.
7: $\quad$ **go to** 2.
8: **else**
9: $\quad$ Exit

3.1 Generalized eigen-deformation modes for fracture and compaction band (Algorithm 2)

The propagation of both crack and compaction band requires dissipating a specific amount of energy to create new crack surfaces or advance compaction zones. As reported in Baud et al. [2004], Rudnicki and Sternlof [2005], Rudnicki [2007], this energy may vary, depending on the type of kinematic modes. In the proposed framework, we assume that the elastic responses are isotropic and the stress and strain tensor are co-axial.

The proposed eigen-erosion framework distinguishes the tensile and compressive contributions of the effective elastic strain energy density in an intact element, following the idea by Miehe et al. [2010]:

$$\begin{aligned} W_{\text{eff}}(\boldsymbol{\varepsilon}) &= W_{\text{eff}}^+(\boldsymbol{\varepsilon}^+) + W_{\text{eff}}^-(\boldsymbol{\varepsilon}^-) \\ &= \frac{1}{2}\boldsymbol{\sigma}^+ : \boldsymbol{\varepsilon}^+ + \frac{1}{2}\boldsymbol{\sigma}^- : \boldsymbol{\varepsilon}^-. \end{aligned} \tag{11}$$

The tensile and compressive split of the strain and stress tensor writes:

$$\begin{aligned} \boldsymbol{\varepsilon} = \boldsymbol{\varepsilon}^+ + \boldsymbol{\varepsilon}^- &= \sum_i < \varepsilon_i >_+ \boldsymbol{n}_i \otimes \boldsymbol{n}_i + \sum_i < \varepsilon_i >_- \boldsymbol{n}_i \otimes \boldsymbol{n}_i; \\ \boldsymbol{\sigma} = \boldsymbol{\sigma}^+ + \boldsymbol{\sigma}^- &= \sum_i < \sigma_i >_+ \boldsymbol{n}_i \otimes \boldsymbol{n}_i + \sum_i < \sigma_i >_- \boldsymbol{n}_i \otimes \boldsymbol{n}_i, \end{aligned} \tag{12}$$

where ε_i and σ_i are eigenvalues, $\boldsymbol{n}_i$ are associated eigenvectors common to $\boldsymbol{\varepsilon}$ and $\boldsymbol{\sigma}$. The bracket operators $< x >_+$ and $< x >_-$ are defined as:

$$< x >_+ = \frac{x + |x|}{2}, \; < x >_- = \frac{x - |x|}{2}. \tag{13}$$

Note that, in addition to the particular form of tensile and compressive splitting we used in this paper, other splitting methods for stress and strain also exist and have been adopted for variational approaches to fracture in the literature. For example, the strain energy could be decomposed into volumetric and deviatoric parts, as suggested in Clayton and Knap [2014] and recently in Mitchell et al. [2016]. Presumably, separating the volumetric and deviatoric contributions of strain energy may make it more convenient to

capture the pressure-sensitive behavior. For instance, one may allow bulk and shear modulus to have different residual values or partition the amount of energy contribution of deviatoric responses used to form compaction band and fracture by introducing the proper material parameters. These options will be further investigated in future study.

On the bases of field and laboratory data, Sternlof et al. [2005] idealize compaction bands as highly eccentric and asymmetric ellipsoidal zones within which porosity loss induced by grain crushing takes place. The direction of the band is perpendicular to the maximum remote compressive stress. Since the aspect ratio of the compaction bands is of order $10^{-3} - 10^{-4}$ [Sternlof et al., 2005], we ignore the elliptical geometry and represent the band by tabular zones of "eroded" elements, similar to the crack geometry. The pore collapse and grain crushing result in significant uniform uniaxial inelastic compactive strain $\varepsilon_{\text{inel}} = -0.1$ inside the band. This literature also states that the elastic property of the band, although differing from the surrounding intact solid matrix, has little effect on the stress state adjacent to the band with large $\varepsilon_{\text{inel}}$ and shear modulus. Thus we adopt the same elastic property for compaction bands in this study for simplification.

The detection of propagation of anti-crack requires the estimation of compressive strain energy dissipation per unit advance of compaction band. Rudnicki and Sternlof [2005] analytically investigated the propagation of an isolated semi-infinite compaction band and proposed that the strain energy density released is simply $\sigma_{\text{ahead}}\varepsilon_{\text{inel}}$ when the elastic modulus of the compaction band remains the same as the surrounding intact porous media. σ_{ahead} is the compressive stress far ahead of the anti-crack tip and $\varepsilon_{\text{inel}}$ is the uniaxial inelastic compactive strain in the band. In the proposed eigen-fracture finite element framework, assuming that the anti-crack process zone is negligibly small, the strain energy released by converting an intact element to compaction band element equals to $\int_{\Omega_e} \min(< \sigma_i >_-) \cdot \varepsilon_{\text{inel}}\, dV$, where $\min(< \sigma_i >_-)$ is the maximum compressive stress and Ω_e is the domain of the element. On the basis of field observation and the data collected in the Aztec Sandstone formation, previous works such as [Sternlof et al., 2005, Rudnicki and Sternlof, 2005] and the experimental work done by Vajdova and Wong [2003], Baud et al. [2004], Stanchits et al. [2009], Charalampidou et al. [2014], a general agreement is that compaction band can be idealized as a Griffith-type flaws that propagates *nearly uniform uniaxial plastic strain*. After the formation, the compaction band is best described as an elastic inclusion embedded within an elastic host matrix.

Fig. 3 presents the idealized stress-strain relation along the principal direction $\boldsymbol{n}_{CB}$ associated with $\min(< \sigma_i >_-)$. During the compaction band formation process, the element undergoes an inelastic strain of -0.1 while the stress remains the same, representing a perfect-plastic constitutive behavior. The associated strain energy (hatched square area in Fig. 3(a)) is released and causes the pore collapse and grain crushing at the grain scale. Collectively, these mechanisms lead to the formation of compaction band. After the formation, a compaction band, which is composed of the compacted and sometime fragmented grains due to pore collapses and grain crushing (see Figure 1), can be viewed as an elastic inclusion, which is capable of locally storing elastic energy without plastic dissipation.

Based on the assumption that the compaction band may be idealized as anti-crack whose propagation may lead to the development of nearly uniform plastic strain in a narrow zone, the eigen-deformation field inside the compaction band element takes the form of a rank-one tensor, i.e.,

$$\boldsymbol{\varepsilon}^* = \boldsymbol{\varepsilon}_{\text{inel}} = \varepsilon_{\text{inel}} \boldsymbol{n}_{CB} \otimes \boldsymbol{n}_{CB}, \tag{14}$$

where we set $\varepsilon_{\text{inel}} = -0.1$ in the numerical example sections. Assuming that the elastic response of the porous media is approximately linear, the constitutive law of the compaction band therefore reads [Sternlof et al., 2005],

$$\boldsymbol{\sigma} = \boldsymbol{\mathcal{C}}^e : (\boldsymbol{\varepsilon} - \boldsymbol{\varepsilon}_{\text{inel}}). \tag{15}$$

Hence this element incorporates the local porosity reduction inside the compaction band by re-setting the referred equilibrium strain to be the eigen-deformation $\boldsymbol{\varepsilon}_{\text{inel}}$. This treatment is in analogy to the sequence of cutting-and-welding operations used by Eshelby to predict the elastic field [Eshelby, 1957, Sternlof et al., 2005, Katsman and Aharonov, 2006, Rudnicki, 2011], where the element for compaction is first removed from the elastic body and then irreversibly and uniaxially shortened. Traction is then applied to the compacted element in order to restore its geometry before removal. Finally, the stretched element is re-inserted back to the surrounding solid and to compute the complete stress field.

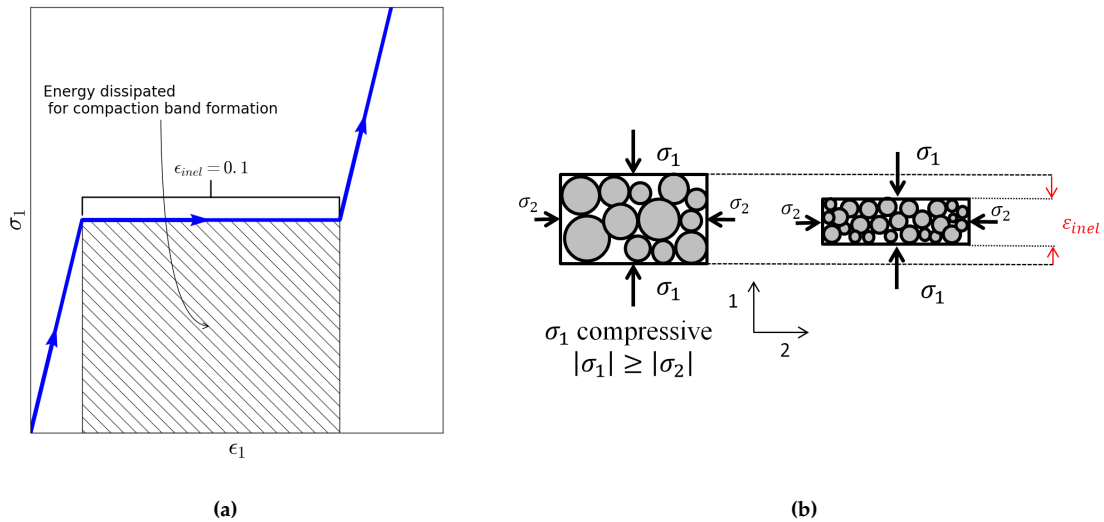

Fig. 3: Compaction band (anti-crack) model. (a) uniaxial stress-strain relation of compaction band. Assume $\sigma_1 = \min(< \sigma_i >_-)$ and set compactive stress and strain as positive value. (b) porosity reduction of compaction band element.

3.2 Transverse isotropic permeability: Nonlocal and local hydraulic aperture algorithm

As the propagation of fracture and compaction band triggers changes in the size and geometry of void space, they may also affect the effective permeability of the porous media. In addition to the change in the magnitude of the permeability, the localized damage zones may also change the flow paths and induce anisotropy of the effective permeability. The permeability changes as well as the induced anisotropy can be incorporated in a double-permeability model [Pride and Berryman, 2003, Choo et al., 2016] or captured explicitly [Foster and Nejad, 2013, Miehe and Mauthe, 2016]. In either case, we assume that the flow inside the fracture and in the host matrix obeys the Darcy's law, i.e.,

$$\bar{\boldsymbol{q}} = -\frac{1}{\mu}\boldsymbol{k}\,\nabla^{\boldsymbol{x}}\,p \tag{16}$$

where $\bar{\boldsymbol{q}}$ is the Darcy velocity, μ is the dynamic viscosity (with the unit of pressure times time) and $\boldsymbol{k}$ is the permeability tensor (with the units of area). We idealize that the localized permeability change due to the presence of compaction band and fracture is of rank-one. In the case of fracture mode, the effective permeability along the flow direction inside the fracture k_f is related to the fracture opening (hydraulic aperture) w via the cubic law. As pointed out in previous work, such as Witherspoon et al. [1980], Zimmerman and Yeo [2000], the local cubic law is only valid when the Reynolds number is sufficiently low such that the transmissivity is independent of flow rate and proportional to the cube of the mean hydraulic aperture w. The cubic law for three-dimensional space takes the following form,

$$\bar{\boldsymbol{q}}\cdot\boldsymbol{t} = -\frac{k_f}{\mu}(\nabla^{\boldsymbol{x}}\,p\cdot\boldsymbol{t}) = -\frac{w^3}{12\mu}(\nabla^{\boldsymbol{x}}\,p\cdot\boldsymbol{t}) \tag{17}$$

where $\boldsymbol{t}$ is the unit vector parallel to the fracture line. In two-dimensional cases where one assumes that the crack is also two-dimensional, the cubic law is often rewritten such that,

$$\bar{\boldsymbol{q}}\cdot\boldsymbol{t}/b = -\frac{k_f}{b\mu}(\nabla^{\boldsymbol{x}}\,p\cdot\boldsymbol{t}) = -\frac{w^2}{12\mu}(\nabla^{\boldsymbol{x}}\,p\cdot\boldsymbol{t}) \tag{18}$$

Algorithm 2 Crack & Compaction band algorithm

Require: Crack set C_n and anti-crack set CB_n at time t_n
Require: Priority queue of crack PQ_C and anti-crack PQ_{CB}.
Set $PQ_C = PQ_{CB} = \emptyset$.
for all elements K not in $C_n \cup CB_n$ **do**
  for all integration points p of K **do**
    Spectral decomposition and tensile/compressive split of current strain and stress tensor: $\boldsymbol{\varepsilon}^+$, $\boldsymbol{\varepsilon}^-$, $\boldsymbol{\sigma}^+$ and $\boldsymbol{\sigma}^-$ (Eq. 12).
    Compute the inelastic compressive strain tensor $\boldsymbol{\varepsilon}_{inel}$ (Eq. 14).
  Compute elastic energy release

$$-\Delta E_K^+ = \int_{\Omega^K} \frac{1}{2}\boldsymbol{\sigma}^+ : \boldsymbol{\varepsilon}^+ \, dV$$

$$-\Delta E_K^- = \int_{\Omega^K} \boldsymbol{\sigma}^- : \boldsymbol{\varepsilon}_{inel} \, dV$$

  Compute effective anti-crack area increment ΔA_K.
  Compute net energy gain

$$-\Delta F_K^+ = -\Delta E_K^+ - G_C \Delta A_K$$

$$-\Delta F_K^- = -\Delta E_K^- - G_{CB} \Delta A_K$$

  If $-\Delta F_K^+ \geq 0$, push K into PQ_C, if $-\Delta F_K^- \geq 0$, push K into PQ_{CB}.
if $PQ_C \neq \emptyset$ **then**
  Pop from PQ_C elements K with $-\Delta F_K^+$ within TOL of largest, add to C_{n+1}.
if $PQ_{CB} \neq \emptyset$ **then**
  Pop from PQ_{CB} elements K with $-\Delta F_K^-$ within TOL of largest, add to CB_{n+1}.
Exit.

where b is the depth of the 2D domain, which is often set as 1 for convenience purpose and hence $k_f = w^2/12$ [Khoei et al., 2014]. The enhanced effective permeability due to the presence of fracture $\boldsymbol{k}_f$ is a rank-one tensor

$$\boldsymbol{k}_f = k_f \boldsymbol{t} \otimes \boldsymbol{t}. \tag{19}$$

The total effective permeability can be idealized as the summation of the isotropic effective permeability of the host matrix and the anisotropic enhancement, i.e.,

$$\boldsymbol{k}_{\text{total}} = \boldsymbol{k}_{\text{host}} + \boldsymbol{k}_f = k\boldsymbol{I} + k_f \boldsymbol{t} \otimes \boldsymbol{t}, \tag{20}$$

where k is the magnitude of the effective permeability of the host. Note that cubic law is commonly used in adjunct to hydro-mechanical models that model fractures via embedded strong discontinuities (e.g. [Foster and Nejad, 2013, de Borst, 2016]) where the mechanical aperture can be computed easily. In the case where the cracks are represented by binary or regularized level set functions, a numerical algorithm must be used to keep track of the orientation and magnitude of the opening at each integration point of the finite element such that the proper permeability enhancement can be computed [Miehe and Mauthe, 2016].

In this work, we propose two numerical algorithms designed specifically for the eigen-fracture model to estimate the hydraulic aperture and the orientation of the crack opening such that the enhanced effective permeability tensor can be estimated properly.

3.2.1 Local hydraulic aperture algorithm

To obtain the hydraulic aperture w and the orientation of the crack opening properly, one possible way is to project the element-wise binary indicator function onto a scalar field with sufficient smoothness (i.e. C^o continuity), which we denoted as d_{eroded}. This field indicates the state of porous media by assigning

value 1 to completely eroded (fractured) material and value 0 to intact material. The simplest approach to construct this field in the eigen-erosion framework is setting $d_{eroded} = 1$ at all nodes of the eroded elements and $d_{eroded} = 0$ for the rest of the finite element nodes (cf. Fig. 4(a)).

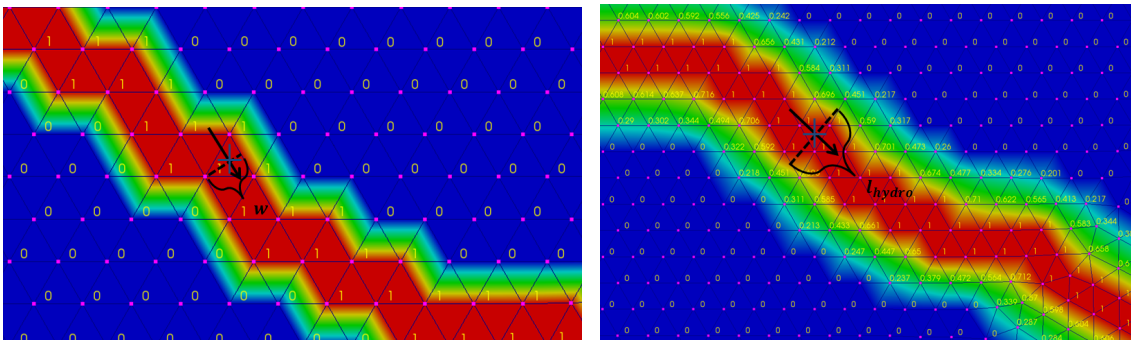

(a) Local scheme **(b)** Nonlocal scheme

Fig. 4: Determination of hydraulic aperture. Local and nonlocal projection of erosion field.

The resulting field may have gradient strongly depending on the finite element mesh size. As the mesh is refined, the gradient across the intact and broken domain may become sharper. However, since we only use the orientation of the gradient field to determine the aperture direction, the mesh sensitivity of the magnitude of the gradient field does not directly impose any difficulty. Furthermore, if the thickness of the crack is only of one element, then one may compute the enhanced permeability by computing the elongation along the orthogonal vector of this gradient field. We refer the numerical scheme based on this design as the "local scheme" (cf. Algorithm 3). In this case, we consider that the direction $\boldsymbol{n}$ normal to the crack is always aligned with the gradient of the erosion field, i.e., $\boldsymbol{n} = ||\nabla d_{eroded}||$. Since the field is constant inside the eroded element, the gradient inside the closest neighboring element is adopted if the finite element is surrounded by broken elements. The unit vector of the flow direction $\boldsymbol{t}$ is perpendicular to the direction vector $\boldsymbol{n}$. An aperture line is then defined along the direction $\boldsymbol{n}$ intercepted by the integration (Gauss) point of the eroded element. The initial length of the aperture line is the distance between the intersection points of this line and the boundary of the eroded elements representing the crack. Meanwhile, the length after the crack opening is obtained using the deformed boundary of the eroded elements. The fracture aperture w is the difference between the deformed length and initial length. In this approach, we assume that the mechanical and hydraulic apertures are identical [Pyrak-Nolte et al., 1987, Renshaw, 1995]. The obvious advantage of this algorithm that it is relatively easy to implement and applicable to both 2D and 3D cases. However, the major drawback is that the amount of energy dissipation of the pore-fluid is sensitive to the mesh size. As further demonstrated in the numerical examples of Section 4, this mesh sensitivity may have profound effect not only one the predicted hydraulic properties but also on the resultant crack and compaction band patterns, due to the hydro-mechanical coupling effects.

3.2.2 Non-local hydraulic aperture algorithm

Experimental studies have long confirmed that the mechanical aperture, defined as the distance between the two opposite faces of a crack, is not identical to the hydraulic aperture – the aperture used in the cubic laws. This discrepancy is commonly observed in experimental work on single-fracture flow and often attributed to the surface roughness, local tortuosity, contact area and the nonlinearity effect at high Reynolds numbers. Consequently, directly applying mechanical aperture in the cubic law generally leads to overestimation of Darcy's velocity [Witherspoon et al., 1980, Pyrak-Nolte et al., 1987, Renshaw, 1995, Chen et al., 2000]. As a result, we design and introduce a nonlocal permeability model which incorporates the length scale of the hydraulic aperture, through an additional neighborhood zone (referred as hydraulic neighborhood ϵ_{hydro} herein) to distinguish the difference between the mechanical and hydraulic apertures.

Algorithm 3 Hydraulic aperture algorithm (local)

Require: Crack set C_n at time t_n
Require: Erosion field d_{eroded} at time t_n
for all elements K in C_n **do**
  Compute gradient of erosion field: ∇d_{eroded}.
  Compute aperture direction: $\boldsymbol{n} = \frac{\nabla d_{eroded}}{||\nabla d_{eroded}||}$.
  Compute flow direction $\boldsymbol{t}$: $\boldsymbol{t} \perp \boldsymbol{n}$.
  Determine the two intersection points between the boundary of C_n. by drawing a line parallel to $\boldsymbol{n}$ and intersected by the (Gauss) integration point p.
  Compute fracture aperture w as the Euclidean distance between the two end points.
  Compute fracture permeability $\boldsymbol{k}_f$ via the cubic law.
  Update total permeability: $\boldsymbol{k}_{\text{total}} = \boldsymbol{k}_{\text{host}} + \boldsymbol{k}_f$
return $\boldsymbol{k}_{\text{total}}$

In this second approach, we first project the discrete indicator function into a smooth field. In other words, the field d_{eroded} inside the ϵ-neighborhood region is obtained by solving the second-order Euler equation (cf. [de Borst and Verhoosel, 2016]):

$$d_{eroded} - l_{hydro}^2 \Delta d_{eroded} = 0, \tag{21}$$

with the boundary conditions that $d_{eroded} = 0$ for nodes at the boundary of the ϵ-neighborhood of the crack and $d_{eroded} = 1$ at all nodes of the eroded elements (cf. Fig. 4(b)). $d_{eroded} = 0$ outside the ϵ-neighborhood region. l_{hydro} is the length scale parameter of hydraulic aperture. The normal direction $\boldsymbol{n}$ is determined from the average of gradients inside the neighboring elements. The hydraulic aperture is computed by:

$$w = A\ l_{hydro}\ \boldsymbol{n} \cdot \boldsymbol{\varepsilon} \cdot \boldsymbol{n}, \tag{22}$$

where $A \in]0, 1]$ is a material parameter related to the difference between the mechanical and hydraulic aperture, which we set it equal to 1 in the examples presented in Section 4. Note that the upper bound 1 implies that the hydraulic aperture is equal or smaller than the mechanical aperture. This scheme is referred to as "nonlocal scheme" (cf. Algorithm 4). Note that this erosion field resembles the phase field in the phase-field method. Subsequently, the total permeability tensor is obtained by $\boldsymbol{k}_{\text{total}} = \boldsymbol{k}_{\text{host}} + \boldsymbol{k}_f$, where $\boldsymbol{k}_{\text{host}}$ is the isotropic permeability tensor for intact porous matrix.

In addition, for elements inside "l_{hydro}-neighborhood" of crack set C (in analogy to "ϵ-neighborhood" except that l_{hydro} is the search radius), they possess reduced fracture permeability: $d_{eroded}^2 \boldsymbol{k}_f$. For each of these elements, an aperture line is defined by its integration point and the gradient of erosion field ∇d_{eroded}. The element in C who has the minimum distance from the element center to the aperture line could be determined. Then the corresponding $\boldsymbol{k}_f$ is used for reduced permeability calculation.

3.2.3 Permeability reduction due to formation of compaction band

If one assumes that the permeability reduction of the compaction band is isotropic inside the compaction band, then the reduction of effective permeability inside the compaction band can be captured by the Kozeny-Carman equation. The rationale behind this assumption is due to the fact that the compaction band, once it is formed, is idealized as an inclusion of isotropic elastic constitutive responses. Hence, we assume that the permeability reduction inside the compaction band is also isotropic for consistency. Note that the inclusion of the permeability reduction inside the compaction band may still lead to anisotropic hydraulic responses at the specimen scale. Improvement of constitutive law that better captures the induced anisotropy of permeability inside compaction band is an important task and will be considered in future study when further experiment evidence and meso-scale data becomes available. The Kozeny-Carman equation [Bear, 1972] relates the effective permeability k with the current void ratio e of porous media, i.e.,

$$k = \frac{d_p^2}{180\mu} \frac{e^3}{(1+e)^2}, \tag{23}$$

Algorithm 4 Hydraulic aperture algorithm (regularized)

Require: Crack set C_n at time t_n
H_1 projection of erosion field d_{eroded} using a length parameter l_{hydro} for hydraulic aperture (Eq. 21).
for all elements K in C_n **do**
    Compute gradient of erosion field: ∇d_{eroded}.
    Compute aperture direction: $\boldsymbol{n} = \frac{\nabla d_{eroded}}{||\nabla d_{eroded}||}$.
    Compute elongation along $\boldsymbol{n}$: $\varepsilon_{\perp} = \boldsymbol{n} \cdot \boldsymbol{\varepsilon} \cdot \boldsymbol{n}$
    Compute aperture: $w = l_{hydro} \cdot \varepsilon_{\perp}$
    Compute fracture permeability $\boldsymbol{k}_f$ via the cubic law.
    Update total permeability: $\boldsymbol{k}_{\text{total}} = \boldsymbol{k}_{\text{host}} + \boldsymbol{k}_f$
for all elements within l_{hydro}-neighborhood of C_n **do**
    Get the closest element K in C_n and the corresponding fracture permeability $\boldsymbol{k}_f$.
    Update total regularized permeability: $\boldsymbol{k}_{\text{total}} = \boldsymbol{k}_{\text{host}} + d^2_{eroded}\boldsymbol{k}_f$.
return $\boldsymbol{k}_{\text{total}}$

where d_p is the particle diameter and the coefficient $\frac{d_p^2}{180\mu}$ holds constant during deformation of the porous media. If the effective permeability takes the value k_0 at the initial void ratio e_0, k can be updated as:

$$k = \left(\frac{e^3}{1+e} / \frac{e_0^3}{1+e_0}\right) k_0. \tag{24}$$

Assuming that the compressibilities of both the solid and fluid constituents are significantly higher than that of the solid skeleton, the change of the void ratio is a function of volumetric strain rate $\dot{\varepsilon_v}$, i.e.,

$$\dot{e} \approx \frac{e_0(1+e)^2}{1+e_0}\dot{\varepsilon_v}, \tag{25}$$

which is obtained by considering the relationships among variables for porous media, i.e.,

$$\dot{e} = \frac{\partial e}{\partial \phi}\dot{\phi} \ ; \ e = \frac{\phi}{1-\phi} \ ; \ \phi \approx (1+\epsilon_v)\phi_0 \tag{26}$$

where ϕ represents the porosity and ϕ_0 is the initial porosity of the porous medium.

Finally, it should be noted that it is possible to use the fracture model to impose a rank-one permeability reduction due to the compaction band.

4 Numerical Examples

In this section, we present three sets of numerical experiments designed to demonstrate the salient features of the proposed model and access the robustness and accuracy of the numerical schemes designed to replicate the onset and propagation of the compaction band and brittle fracture. In the first example, we simulate the hydro-mechanical coupling effect of solid deformation, fracture nucleation and induced fluid flow occurred in a notch specimen subjected to different combinations of tensile, shear and compression loads. By varying the prescribed loading, tensile fracture, mixed-mode fracture and compaction band/anti-crack are nucleated from the notches and propagate in different directions. By conducting the same simulations with different meshes, we assess the mesh sensitivity of the proposed scheme. In the second set of numerical simulations, we attend to simulate the borehole breakout problem commonly encountered in the drilling process due to preferential rock failure. In particular, this example demonstrates the potential of using a unified framework to model compaction band and brittle fracture to analyze and predict the potential breakout. In the final set of numerical simulations, we simulate a series of injection simulations in homogeneous and heterogeneous porous media. The simulations showcase the ability of the unified eigen-erosion framework to capture the propagation and coalescence of fracture and compaction

band and the corresponding effects on the flow patterns due to the interaction of fracture and compaction bands. For simplicity, we assume that the elastic moduli of the compaction band as an inclusion and the host matrix are identical.

4.1 Tension/compression shear tests on fluid-saturated double-edge-notched specimen

In this first example, we investigate the onset and propagation of cracks and compaction bands inside a fluid-saturated specimen under different loading conditions. The geometry of the specimen is identical to the double-edge-notched specimen used in a Nooru-Mohamed shear experiment originally designed for analyzing mixed-mode fractures in concrete specimen [Nooru-Mohamed, 1992]. The specimen is assumed to be under the plane strain condition. The thickness of the specimen is 1000 mm. The domain and the boundary conditions, as well as a coarse and a fine mesh of 3-node triangular elements are all depicted in Fig. 5. The center of the specimen is constrained in X and Y directions to prohibit rigid body displacement. At the first loading step, a traction P_s is applied to the upper-left and lower-right edges of the specimen, with no crack or compaction band triggered. To replicate the experimental setup these two edges are maintained to stay straight throughout the simulation via the usage of a Lagrangian multiplier. The loading rate is first set to be negligibly low so that the excess pore pressure built up inside the specimen is small compared to the applied loading to resemble a fully drained condition. Subsequently, the top and bottom edges are subjected to constant loading rate, while maintaining the same pressure P_s. The material parameters adopted in this example are recapitulated in Table 1.

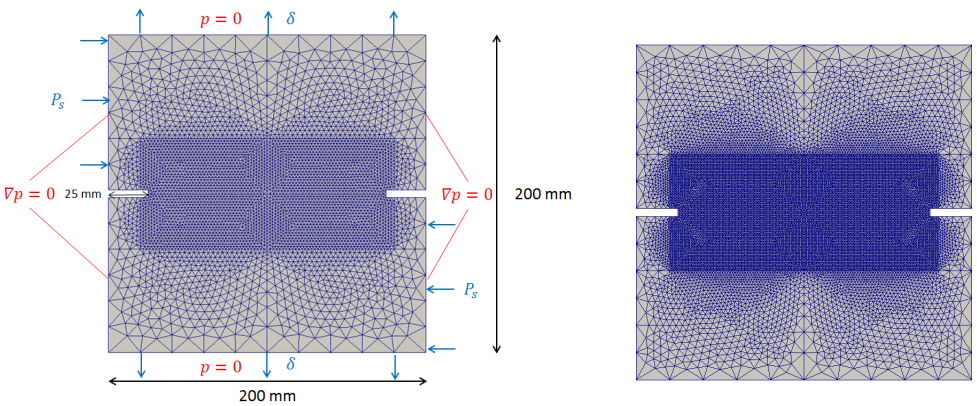

(a) Coarse mesh, 4 539 nodes, 8 992 elements **(b)** Fine mesh, 16 649 nodes, 33 200 elements

Fig. 5: Geometry, boundary condition and mesh

4.1.1 Effect of critical energy release rate of compaction band

The first loading condition consists of 15 MPa pressure for constant shear load and a tensile loading strain rate of 0.0005 s^{-1} for both the top and bottom edges. As reported from the literature (e.g. Sternlof et al. [2005], Stanchits et al. [2009], the critical energy release for compaction band varies due to the difference in mineral composition, initial porosity and the types of materials. Nevertheless, previous studies have confirmed that the typically critical energy release rate for compaction band may range from 10 kJ/m^2 to 80 kJ/m^2 and is typically higher than the critical energy release rate of fracture. To analyze how the difference in the critical energy release rate of fracture and compaction affects the fracture and compaction band patterns, we run a simulation with material parameters all identical to the one reported in Table 1 except the critical energy release rate is cut by half. Fig. 6 compare the predicted crack path with two critical energy release rate for compaction band while keeping the same critical energy release rate for fracture.

Parameter	Value
Solid matrix Young's modulus E	20 GPa
Solid matrix Poisson's ratio ν	0.2
Critical energy release rate of crack G_C	$1\ kJ/m^2$
Critical energy release rate of compaction band G_{CB}	$20\ kJ/m^2$
Fluid bulk modulus K_f	2.2 GPa
Solid particle bulk modulus K_f	45 GPa
Initial porosity ϕ	0.25
Biot's coefficient B	0.75
Biot's modulus M	8 GPa
Intrinsic permeability κ	$1e^{-13}\ m^2$
Dynamic viscosity μ	$1e^{-3}\ Pa \cdot s$
Length scale parameter for crack	$\epsilon_C = 0.005$ m
Length scale parameter for anti-crack	$\epsilon_{CB} = 0.005$ m
Length scale parameter for hydraulic aperture	$l_{hydro} = 0.0025$ m

Table 1: Material parameters for double-edge-notched specimen

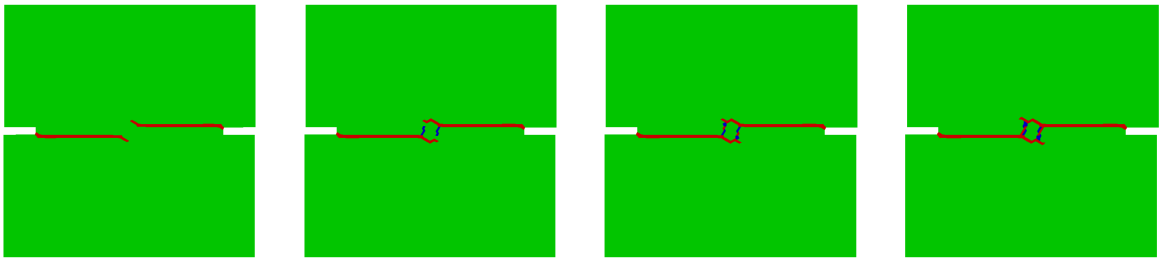

(a) $G_{CB} = 10\ kJ/m^2$

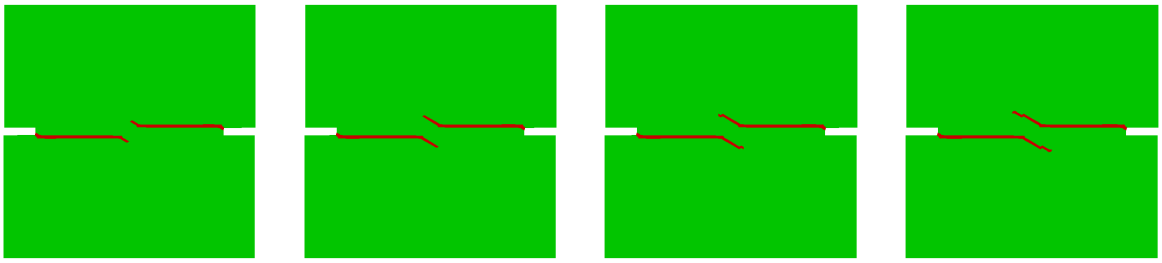

(b) $G_{CB} = 20\ kJ/m^2$

Fig. 6: Effect of compaction band on crack propagation.
Red: crack set; Blue: compaction band set.

In both cases, fracture forms after the normal traction on the top of the specimen reaches the maximum value. In the simulation where the critical energy release rate for compaction band $G_{CB} = 10\ kJ/m^2$, the combination of shear and tensile load leads to the onset and propagation of cracks from the two notches. As the two cracks propagating from the left and right get close enough, the compressive stress near the crack tip increases and ultimately leads to the formation of compaction bands oriented orthogonal to the existing cracks. Since the stress field in the vicinity of the two crack tips is altered by the formation of compaction bands, the cracks stop extending away from each other, but tend to coalesce. In the other case

in which $G_{CB} = 20\ kJ/m^2$, two cracks simultaneously nucleate from the two notches and approach the specimen center, while no compaction band is initiated. With the presence of mixed shear-tensile loading condition, two cracks deviate from each other and follow inclined paths in the opposite directions. Results from this numerical experiment suggest the possible interactions between cracks and compaction bands when the critical energy release rate for these two Griffith-type flaws are close to each other. To the best knowledge of the authors, this is the first time the interactions between compaction band and fractures have been captured numerically.

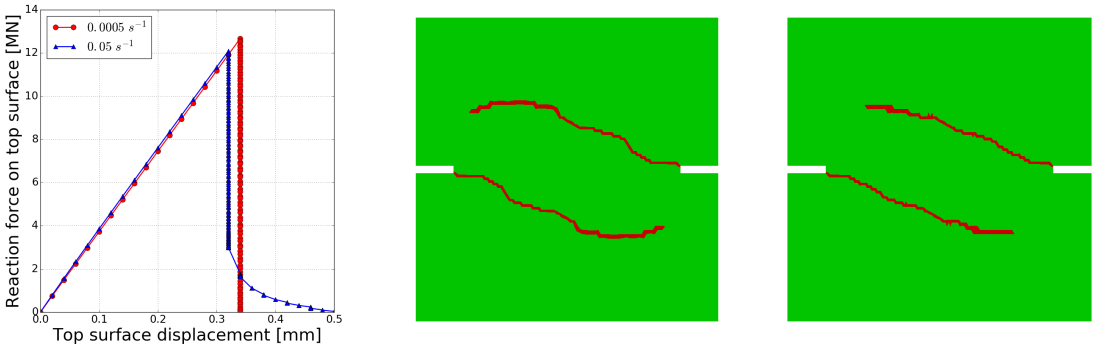

(a) **(b)** strain rate 0.0005 s^{-1} **(c)** strain rate 0.05 s^{-1}

Fig. 7: Effect of tensile loading rate on crack propagation, $P_s = 50$ MPa. (a) Vertical reaction force vs. vertical displacement on the top surface. (b) crack path at strain rate 0.0005 s^{-1}. (c) crack path at strain rate 0.05 s^{-1}.

4.1.2 Fluid-induced rate effects

The pore fluid plays an important role in the mechanical behavior of fluid saturated porous media. Through the hydro-mechanical coupling, [Sun, 2013, Bésuelle and Rudnicki, 2003, Na and Sun, 2016], the solid skeleton constitutive responses may appear to be rate dependent due to the diffusion of pore fluid, even though the solid skeleton itself does not exhibit any rate dependence. To investigate this fluid-induced effect on the crack propagation, we conduct two numerical simulations on the same specimen loaded under two different strain rates i.e. 0.0005 s^{-1} and 0.05 s^{-1}. These strain rates are generated by moving the both top and bottom edges with equal-magnitude, opposite-direction velocity. In both simulations, the side-wall traction remains $P_s = 50$ MPa throughout the numerical test. The load-displacement curve in Fig. 7 shows the force-displacement relation of the specimen subjected to the two different rates. Since a zero-pore-pressure boundary condition is prescribed at the top and bottom edges of the specimen, it is difficult to build up excess pore pressure in the specimen unless a very high loading rate (relative to the hydraulic conductivity) is prescribed. Nevertheless, the hydro-mechanical effect may still manifest in multiple ways. As shown in Fig. 7(a), we observe that the specimen subjected to higher loading rate also appears slightly more stiff. Furthermore, even though we only employ rate-independent models to capture the elastic responses, the maximum normal force on the top is found to be sensitive to the loading rate. Finally, for the case where strain rate is 0.0005 s^{-1}, the reaction force abruptly drops as the cracks evolve to the final configuration within one loading step. This global response differs from the high-strain-rate case in which softening can be observed when the top surface displacement is between 0.3 mm to 0.5 mm. The pore fluid also effect the predicted crack paths in the two cases, as shown in Fig. 7.

Fig. 8 presents the pore pressure and Darcy velocity field predicted by the proposed algorithm for the fractured specimen. Note that the Darcy's velocity plotted in Figs. 8 (c) and (d) are illustrated with a log-scale color scheme. When subjected to a high loading rate (two orders higher than the low-loading rate counterpart), the pore pressure built up within the specimen is also approximately of two orders higher than the low-loading-rate counterpart. The magnitude and direction of Darcy velocity also evolve as the

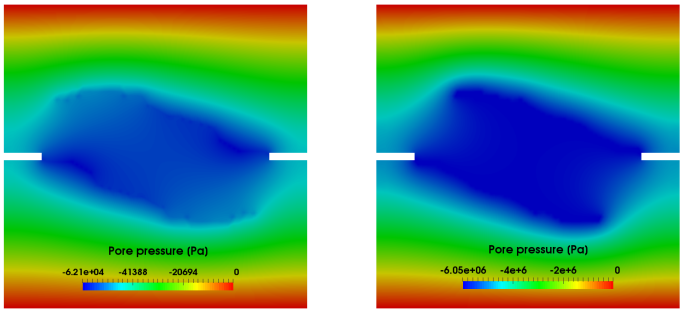

(a) strain rate 0.0005 s^{-1} **(b)** strain rate 0.05 s^{-1}

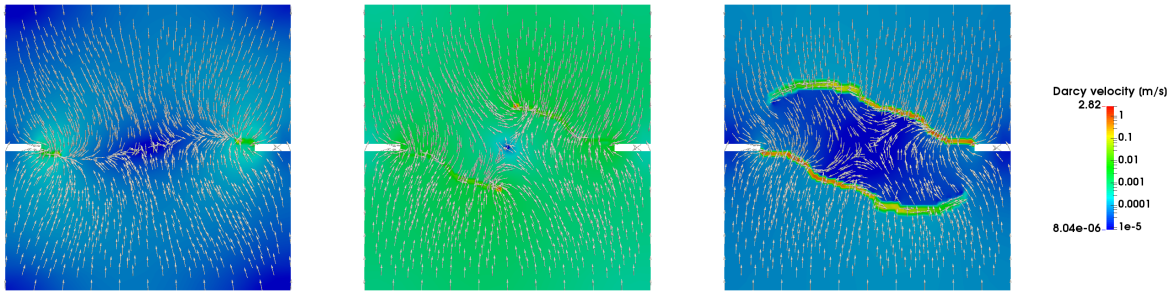

(c) strain rate 0.0005 s^{-1}

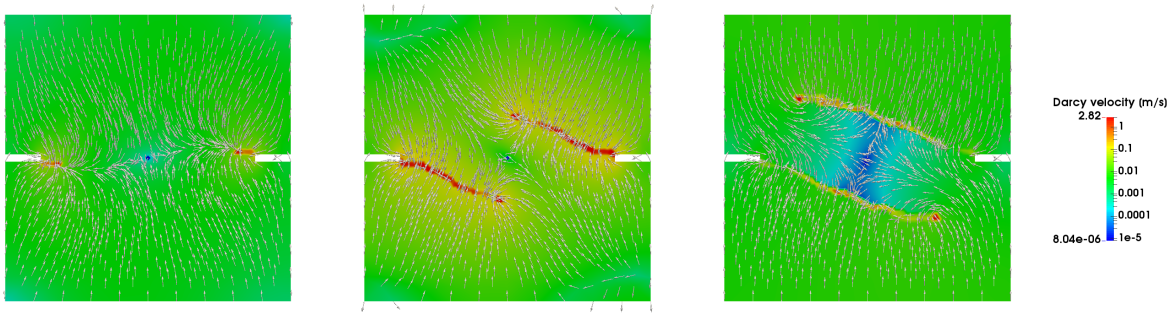

(d) strain rate 0.05 s^{-1}

Fig. 8: Rate effect on the pore pressure and Darcy velocity distribution, $P_s = 50$ MPa. In both case, the cracks acts as flow conduits.

cracks propagate. Water flows into the specimen in tension through the top and bottom boundaries where a pressure head is prescribed. The presence of cracks significantly alters the Darcy velocity field: water tends to flow into the cracks and are stored in the void space near the crack where the pressure plume located. The flow patterns demonstrated in Fig. 8 indicate that the cracks do behave like flow conduits which draws water by creating a fast pathway along the crack propagation direction.

4.1.3 Mechanical and hydraulic apertures

To demonstrate the necessity of adopting the "nonlocal scheme" in computing hydraulic aperture for fractures, we conduct three simulations with different meshes such that a quantitative assessment of the mesh

dependency can be established. In this set of numerical experiments, the nonlocal scheme is applied on both coarse and fine meshes with the same ϵ_C, ϵ_{CB} and l_{hydro}. Meanwhile, the local scheme is applied on fine mesh with the same ϵ_C and ϵ_{CB}, but the hydraulic aperture is assumed to be the same as the crack opening. The boundary conditions and material parameters used in these simulations are also identical.

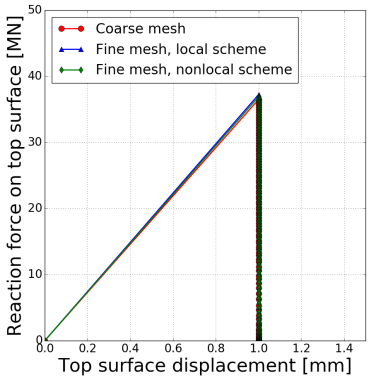

Fig. 9: Mesh dependency: reaction force vs. prescribed vertical displacement on top surface.

Fig. 9 shows the force-displacement curves obtained from the three simulations. These curves are all consistent with those of a brittle materials and their difference is minor. This indicates that the specimen-scale response is not very sensitivity to the meshes. However, a closer examination on the local responses, in particular, the predicted crack paths and the pore pressure field shown in Fig. 10 and Fig. 11 reveals that a pathological bias may occur when the local scheme described in Algorithm 3 is used to compute the hydraulic aperture. On the other hand, the coarse and fine meshes yield similar crack patterns and pore pressure field when the nonlocal scheme described in Algorithm 4 is used.

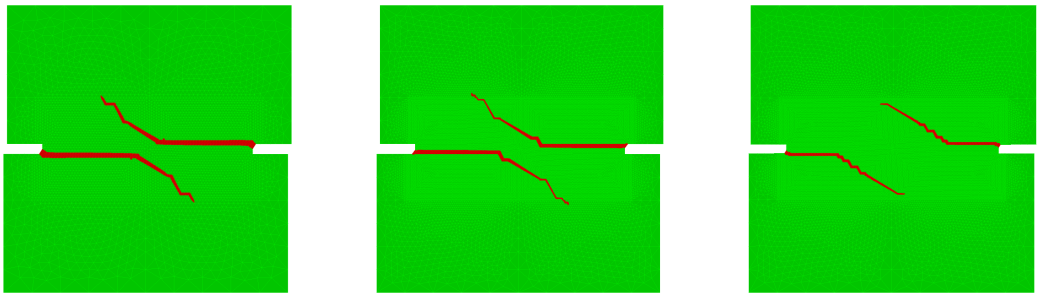

(a) Coarse mesh **(b)** Fine mesh, nonlocal permeability **(c)** Fine mesh, local permeability

Fig. 10: Assessment of mesh dependency: crack path predicted by different meshes and local & nonlocal hydraulic aperture algorithms.

These encouraging results are due to the usage of ϵ-neighborhood (for fracture) and l_{hydro}-neighborhood (for permeability). Since both the size of the ϵ-neighborhood and l_{hydro}-neighborhood are independent of the mesh size, these treatments allows the energy dissipation due to the crack propagation and fluid diffusion regularized by the length scales. Finally, it should be noted that it is possible to introduce a more

comprehensive phenomenological model to relate the hydraulic and mechanical apertures (e.g. Chen et al. [2000]). This research direction is out of the scope of this study but will be considered in the future.

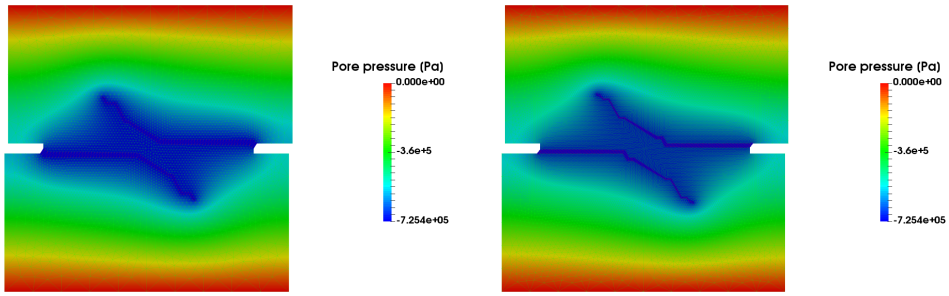

(a) Coarse mesh **(b)** Fine mesh, nonlocal permeability

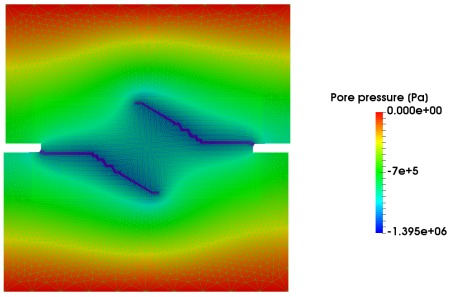

(c) Fine mesh, local permeability

Fig. 11: Assessment of mesh dependency: fluid pressure predicted by different meshes and local & nonlocal hydraulic aperture algorithms.

4.1.4 Shear effect on formation and propagation of compaction bands

In order to initiate and propagate compaction bands, the specimen are compressed under constant shear stress P_s. The magnitude of shear stress effects the anti-crack paths, as shown in Fig. 12. Since the formation of compaction bands results in significant volume reduction compared to surrounding intact porous media, the distribution of volumetric strain is used as the illustration of anti-crack configurations in the figure. Under low shear stress of $P_s = 50$ MPa, the anti-cracks nucleate from the two notches and propagate horizontally and finally merge with each other. With increasing P_s, compaction bands propagate towards the top and bottom edges. This example shows that the unified eigen-fracture scheme is capable of predicting curved compaction band paths.

Fig. 13 demonstrated the direction and magnitude of Darcy velocity field right after the formation of compaction band in the cases where shear loads $P_s = 50$ MPa, 100 MPa, 120 MPa. As opposed to the cases shown in Fig. 8, the formation of compaction bands lead to a flow barrier in which the water inside the compaction band is squeezed out from the compaction band due to the porosity reduction. In all three cases, the Darcy velocity inside the specimen subjected to compression is much lower than the tensile-loading cases where crack propagates.

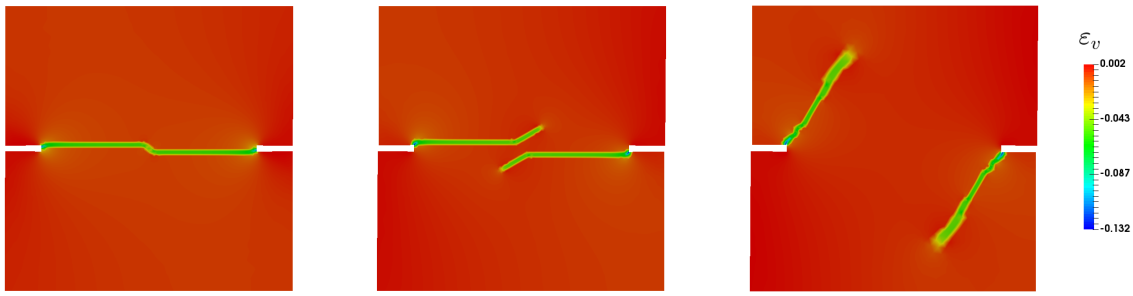

(a) $P_s = 50$ MPa **(b)** $P_s = 100$ MPa **(c)** $P_s = 120$ MPa

Fig. 12: Compaction bands developed inside the specimen during compressive-shear tests subjected to shear loads $P_s = 50$ MPa, 100 MPa, 120 MPa, illustrated by volumetric strain ε_v contour.

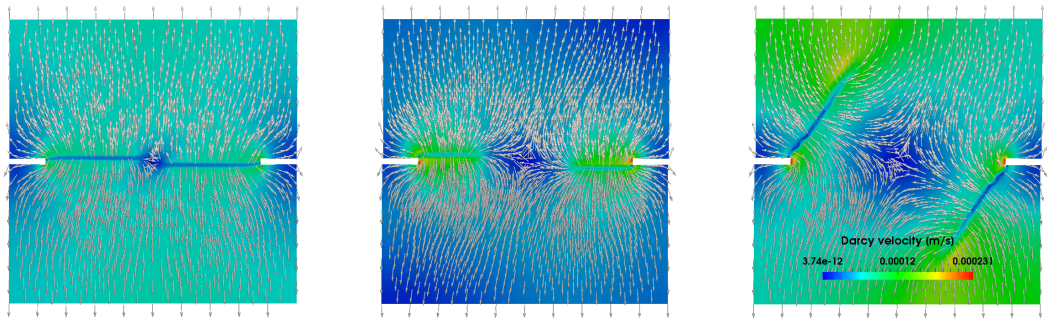

(a) $P_s = 50$ MPa **(b)** $P_s = 100$ MPa **(c)** $P_s = 120$ MPa

Fig. 13: Flow barrier effect of compaction bands developed inside the specimen during compressive-shear tests subjected to shear loads $P_s = 50$ MPa, 100 MPa, 120 MPa, as demonstrated by Darcy velocity field.

4.2 Fracture-like borehole breakout induced by compaction bands

Borehole breakouts are stress-induced enlargements of the wellbore cross-section. The breakout phenomena have been observed in a number of drilling operations, such as breakouts in the Witwatersrand gold mine in South Africa [Leeman et al., 1964] and in the Exploratory Studies Facility below the Yucca Crest, Nevada [Wang and Elsworth, 1999]. In those cases, boreholes often elongate in the direction of the minimum principal stress orthogonal to the borehole axis [Zheng et al., 1989]. While there are a number of conceptual models since the 80s to explain the breakouts as a mechanism due to ex-tensile or shear failure, (cf. Zoback et al. [1985], Haimson and Song [1993]), recent experimental work, such as Haimson [2001], Haimson and Lee [2004], Haimson [2007], have provided a substantial amount of evidence that the borehole breakout in high-porosity rock is due to a sequence of micro-mechanical events described as follows.

1. The formation and propagation of compaction band orthogonal to the maximum principal stress direction.
2. Inside the compaction band, grain crushing and fragmentation causes porosity reduction and creates a narrow zone with compacted fine grains .
3. If the flowing rate of the drilling fluid circulating inside the borehole is very high, then the drilling fluid may flushes out the fine grains inside the compaction band. Otherwise, the fine grains in the compaction band may be partially removed.

4. In the former case, the removal of the fine grains may cause the stress concentration moves and cause the breakout propagation. In the latter case, the partial removal of fine grains creates a weak layer that is vulnerable to fracture.
5. If the flow rate is not high enough to cause the fine grains completely removed but high enough to build up excess pore pressure over time, then a fracture may emerge due to the hydro-mechanical coupling effect.

In this example, our objective is to simulate the low-flow-rate case in which the fine grains in the compaction band are not completely flushed out, but the compaction band is weakened due to the circulation of the drilling fluid, i.e., the un-emptied compaction band case as reported in [Katsman et al., 2009]. To simulate the propagation of the compaction band inside a drilled sandstone specimen, we construct an idealized 2D plane strain boundary value problem considers only half of a rectangular sandstone specimen of dimension 230 mm x 150 mm. A circular hole of radius 11.5 mm has been drilled through the sandstone. The drilled specimen is subjected to a confining pressure of $\sigma_H = 100$ MPa on the long side and $\sigma_h = 40$ MPa on the short side. The material properties of the specimen is identical to the ones shown in Table 1 with the following exceptions: $E = 9.24$ GPa; $\nu = 0.25$; $G_C = 100\ J/m^2$; $G_{CB} = 200\ J/m^2$; $\kappa = 1e^{-17}$ m^2; $\epsilon_C = \epsilon_{CB} = l_{hydro} = 2$ mm. To replicate the experimental procedure, the simulation is designed in two phases. In the first phase, we consider the plane-strain domain with the cylindrical borehole at the center subjected to an anisotropic far-field stress under fully drained condition. This lead to the development of compaction band. Following this, we change the boundary condition such that the drilling fluid begins to inject into the borehole and ultimately leads to the borehole breakout along the compaction band at a sufficiently low injection rate.

4.2.1 Formation of compaction band

At the first phase of the simulation, the presence of borehole under anisotropic far field stress induces the nucleation of the compaction band. Fig. 14 shows the evolution of the binary indicating function of the compaction band (blue color) in selected iteration steps used by the eigen-fracture algorithm to establish equilibrium. Sine we assume that the material remains in drained condition, these iteration steps are not correlated with the time steps. However, Fig. 14 does reveal that the compaction band does propagate along the minimum compressive stress direction, which is consistent with the experimental evidence in [Haimson and Lee, 2004]. This first simulation stage approximates the un-emptied compaction band configuration where the compacted and crushed grains are not evacuated into the borehole by the drilling fluid during the drilling process [Katsman et al., 2009]. The compaction band propagation demonstrated in Fig. 14 is also consistent with the evolution of the stress concentration location (see σ_{yy} field in Fig. 15).

4.2.2 Fractures in compaction bands during fluid injection

At the second stage, water is injected into the borehole to expand the previously formed compaction band. This is realized by discretizing the circular borehole by finite elements and idealizing the flow inside the borehole as a potential flow of incompressible fluid. For clarity, the mesh used to solve the fluid diffusion problem in the borehole is not shown in Fig.16.

Since the grains inside the compaction band are damaged and further weakened by the partial removal of fine grains, we make a highly idealized assumption that the critical energy release rate for crack inside the compaction band is two orders smaller than those formed in the host matrix. Under this hypothesis, fluid will expand and then erode the compaction band elements, forming a crack along the anti-crack path. Notice that a more complete model for the borehole breakout must be able to capture the mass exchange between the intact host matrix and the fine grain suspension in the pore fluid as well as the changes of the elastic constitutive responses due to the removal of fine grains. These details are neglected in this study but will be considered in the future.

Eventually, the configuration will be similar to the borehole breakout experiments [Haimson, 2001, Haimson and Lee, 2004], where highly compacted region lies ahead of the crack tip (c.f Fig. 16). Fig. 17 shows the σ_{yy} field during crack propagation induced by injection of fluid and Fig. 18 illustrates the corresponding pore pressure fields at different time after the injection of water. As expected, the pore pressure

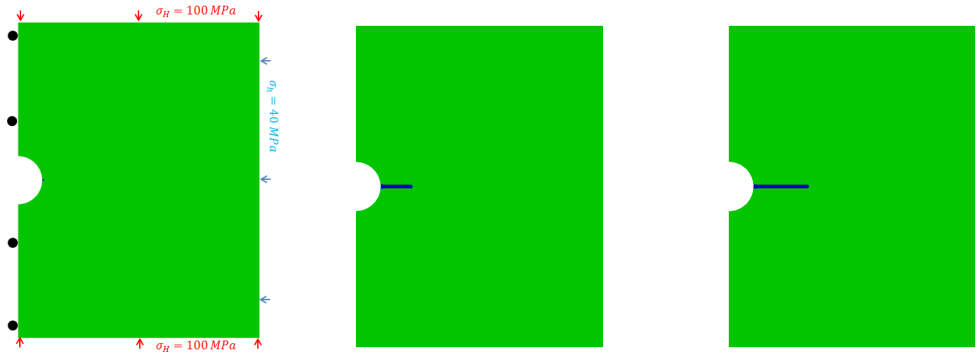

(a) Iteration 1 **(b)** Iteration 30 **(c)** Iteration 53

Fig. 14: First stage of borehole breakout simulation: the presence of borehole in a biaxial stress field induces the onset and propagation of compaction band. The stable compaction band is formed after 53 iterations of the anti-crack tracking algorithm (Section 3) within one time step. The compaction band configurations at the 1st, 30th and 53th iteration are presented to show its propagation. Blue: compaction band set.

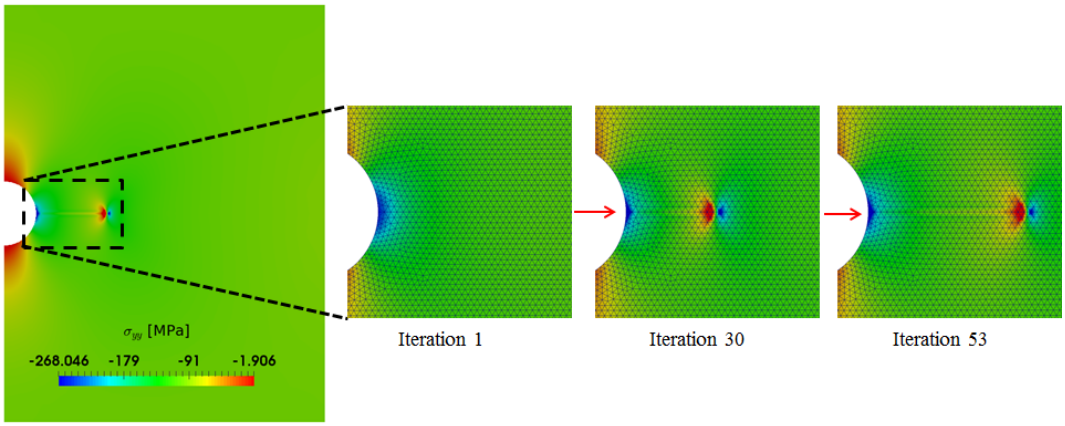

Fig. 15: Distribution of σ_{yy} (stress component along the maximum compressive stress σ_H) during the compaction band formation stage at the 1st, 30th and 53th iteration.

plume grows in the same direction of the crack. As the crack propagates inside the compaction band, the hydraulic aperture increases and this in return causes permeability significantly increases along the crack that was previously the low-permeability compaction band. Note that the assumption of reducing the compaction band G_c in order to achieve this consistency is a significant simplified way to take account of the grain-removal process.

4.3 Coalescence of cracks and compaction band inside a heterogeneous domain

In this last example, we employ the unified eigen-erosion framework to predict the propagation and coalescence of fluid-driven fractures and compaction band in porous media. The interaction between nearby fractures may induce the onset and evolution of compaction bands. This phenomenon has not been observed in real-life field or laboratory experiments, while the numerical results may motivate research in this direction.

We consider a boundary value problem with a water-saturated 20 m x 20 m square domain with three preexisting cracks under plane-strain condition. Fig. 19 presents the domain geometry and initial configuration of the cracks. All cracks have the initial length of 1.2 m, one is embedded horizontally at the domain

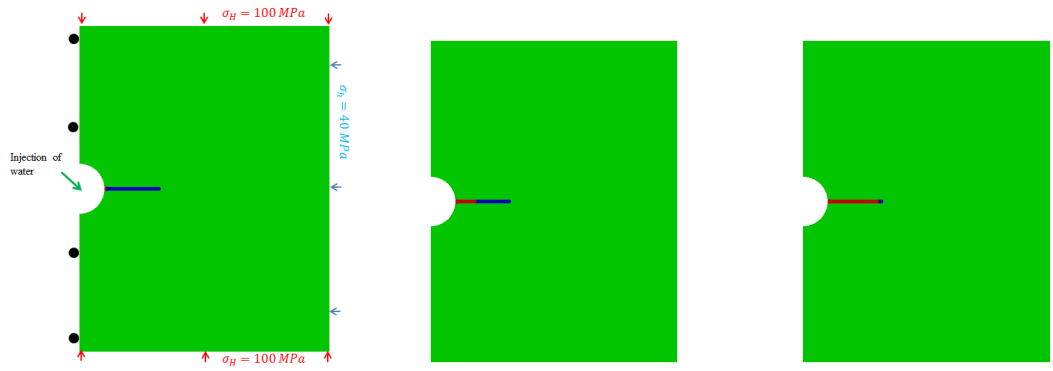

(a) t = 0.2 s after injection **(b)** t = 0.4 s after injection **(c)** t = 0.6 s after injection

Fig. 16: Second stage of borehole breakout simulation: crack of the compaction band upon injection of water into the borehole (prescribed injection velocity $v_{\text{inject}} = 0.001$ m/s at the center node of the borehole, borehole mesh not shown). Crack advances along the anti-crack path, based on the assumption that the grains compaction and crushing largely reduce the G_C of porous matrix inside the compaction band, . Red: crack set; Blue: compaction band set.

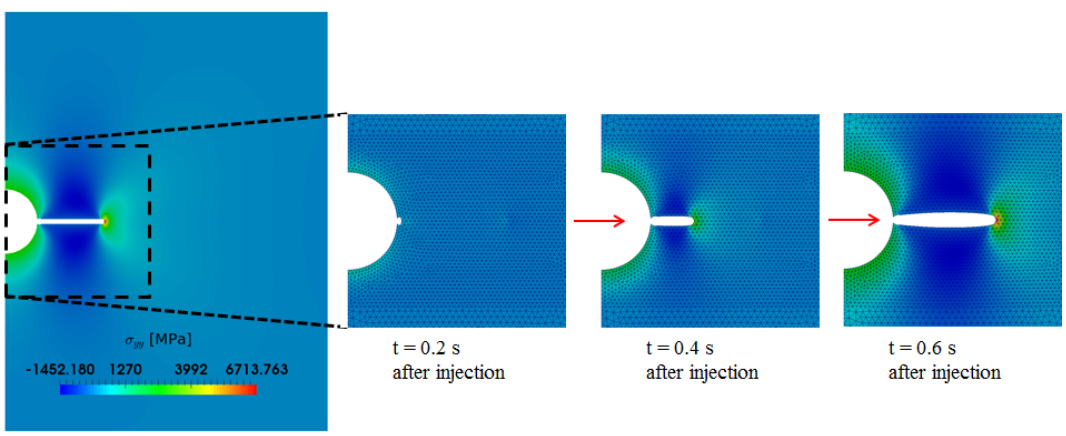

Fig. 17: Distribution of σ_{yy} (stress component along the maximum compressive stress σ_H) during crack propagation induced by injection of fluid along the compaction band path.

center, the other two are oriented vertically 0.75 m apart from the ends of the horizontal crack. The separation between the vertical cracks is 2.7 m. As a result, the domain is symmetric with respect to the central Y-axis.

In the numerical simulations, water is simultaneously injected into the three preexisting cracks through their centers with a prescribed Darcy velocity v_{inject}, driving the cracks to propagate. The center square region of size 4 m x 4 m is discretized by 20,000 triangular elements of size $h_{min} = 0.04$ m. The remaining regions, which are far away from the interaction zone of the cracks, are discretized by larger finite elements as shown in Fig. 19. The displacement along the four edges of the square domain are constrained and the pore pressure is set to 0 Pa along these boundaries. The length scale for crack and compaction band are $\epsilon_C = \epsilon_{CB} = 4h_{min} = 0.16$ m, and the hydraulic length scale is $l_{hydro} = 2h_{min} = 0.08$ m.

To demonstrate the ability of the proposed model to simulate the propagation of cracks and compaction bands without any a priori knowledge of the propagation path, we introduce spatial heterogeneity by generating a random porosity field. Following this step, we then use empirical equations to relate the drained bulk and shear moduli as well as the critical energy release rate for fracture and compaction band

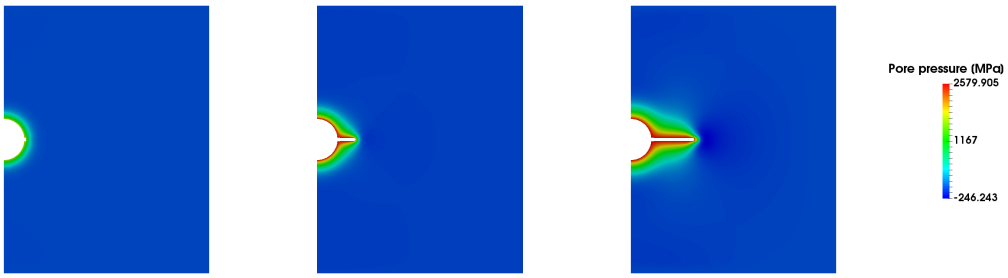

(a) t = 0.2 s after injection **(b)** t = 0.4 s after injection **(c)** t = 0.6 s after injection

Fig. 18: Distribution of pore pressure during crack propagation induced by injection of fluid along the compaction band path.

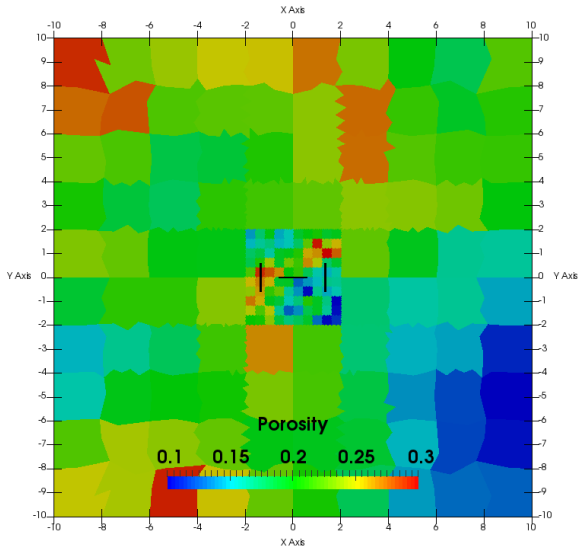

Fig. 19: Embedded cracks (black lines) inside a water-saturated brittle elastic porous medium with randomly generated porosity distribution.

to the porosity [Lee, 2005]. This treatment will gives us an idealized domain of heterogeneous material properties that solely depends on the spatial distribution of porosity.

The heterogeneous porosity field used in the simulation is generated by an open-source multi-scale random field simulation program developed by Baker et al. [2011]. Our goal is to use this program as a code to generate heterogeneous domains. Since it is not our purpose to use the realizations to quantify the effect of the correlation length or the spatial variability via Monte Carlos simulations, the quality of the stochastic realizations and possible improvement of the random-field generation techniques generate non-Gaussian random field is not considered in this study.

Furthermore, we use the mechanical and hydraulic properties of the porous rock specimen with porosity equals to 0.2 as the reference. The corresponding material parameters are listed in Table 2. To generate the heterogeneous domain, we idealized the porosity as a Gaussian random field and set the porosity ranging from 0.1 to 0.3, with mean value of $\phi_0 = 0.2$. A coarse-scale field is first generated with spatial correlation for the 20 m x 20 m domain and the field inside the region of interest of 4 m x 4 m is then refined [Baker et al., 2011]. The resulting porosity field is presented in Fig. 19. The mean value of the resultant porosity field is 0.197 and the standard deviation is 0.0451. With the initial porosity determined, we then obtain the rest of the mechanical and hydraulic material parameters via empirical or phenomenological

Parameter	Value
Solid matrix Young's modulus E	33.68 GPa
Solid matrix Poisson's ratio ν	0.17
Critical energy release rate G_C	100 $Pa \cdot m$
Solid grain bulk modulus K_s	38 GPa
Fluid bulk modulus K_f	2.2 GPa
Biot's coefficient B	0.55
Biot's modulus M	9.9 GPa
Reference permeability κ at 0.2 porosity	$1e^{-15}$ m^2
Dynamic viscosity μ	$1e^{-3}$ $Pa \cdot s$

Table 2: Material parameters for Example 4.3 (porosity $\phi = 0.2$)

.

relations. For instance, The bulk modulus K_ϕ and the shear modulus G_ϕ of rock are related to the porosity ϕ by the empirical equations in Lee [2005]:

$$\begin{aligned} K_\phi &= \frac{K_{\text{quartz}}(1-\phi)}{1+\alpha\phi} \\ G_\phi &= \frac{G_{\text{quartz}}(1-\phi)}{1+\gamma\alpha\phi}, \end{aligned} \tag{27}$$

where the modulus of quartz K_{quartz} = 38 GPa and G_{quartz} = 44 GPa, α is a parameter that represents the degree of consolidation between grains ($\alpha = 4$ in this example) and $\gamma = \frac{1+2\alpha}{1+\alpha}$. The intrinsic permeability depends on the porosity ϕ by the Kozeny–Carman equation, i.e. $\kappa_\phi = \kappa_{\phi_0}\frac{\phi^3}{(1-\phi)^2}$ where $\kappa_{\phi_0} = 8 \times 10^{-14}$ m^2 and $\kappa_\phi = 10^{-15}$ m^2 when porosity $\phi = 0.2$. As for the critical energy release rate for cracks and anti-cracks, they are assumed to follow the power law [Dunn et al., 1973]:

$$\frac{G_{C_\phi}}{G_{C_{\phi_0}}} = \frac{\phi^{n_C}}{\phi_0^{n_C}}; \quad \frac{G_{CB_\phi}}{G_{CB_{\phi_0}}} = \frac{\phi^{n_{CB}}}{\phi_0^{n_{CB}}}. \tag{28}$$

In this example, $G_{C_{\phi_0}} = G_{CB_{\phi_0}} = 100$ $Pa \cdot m$ at the reference porosity ϕ_0, and the parameters $n_C = n_{CB} = -1$. Note that the pressure-dependent rock property and plasticity are not considered in the current simulation.

4.3.1 Fluid-driven fractures in heterogeneous domain

To investigate the effect of the heterogeneity of the porosity field on fluid-driven fracture process, a simulation is firstly performed on homogeneous field with a constant porosity $\phi_0 = 0.2$ and the corresponding homogeneous material properties as a control experiment. The fluid injection velocity is $v_{\text{inject}} = 0.00025$ m/s and the time step is 0.1 s. G_{CB} is set to be 20 kJ/m^2 and no anti-crack is generated during the process. Fig. 20 depicts the evolution of fluid pressure field. Due to the symmetry of the boundary value problem, all crack tips of the three cracks advance in straight lines until the cracks coalesce. The pore pressure inside the horizontal crack is lower than the pore pressure in vertical cracks. This may be attributed to the higher crack propagation speed of the horizontal crack, which reduces the amount of pore pressure built up due to enhancement of permeability along the crack as shown in Fig. 20(a). At $t = 3$ s, the center crack join the vertical cracks at their centers, and the pressure values in the three cracks become nearly identical while the pore pressure plumes originated from the boundaries of the three cracks also joined together to form a single boundary layer domain. This hydromechanical interaction in return causes the crack paths of the vertical cracks to incline. The resultant final crack pattern is consistent with previous results from the crack-coalescence simulations in porous media via the phase field approach [Wheeler et al., 2014, Miehe

and Mauthe, 2016]. As a comparison, the simulation runs again with the identical setting except that the homogeneous porosity field is now replaced by the heterogeneous counterpart. With the same flow injection rate, the pore pressure of the heterogeneous domain at t = 2 s, 3 s, 5 s are shown in Fig. 21 for comparison. In this case, all cracks tend to propagate towards regions where porosity is higher. The final fracture pattern differs significantly from the homogeneous counterpart. The main reason for this discrepancy is that the drop of G_C with increasing porosity facilitates the crack propagation, and this factor dominates the effects of the other porosity-dependent material properties.

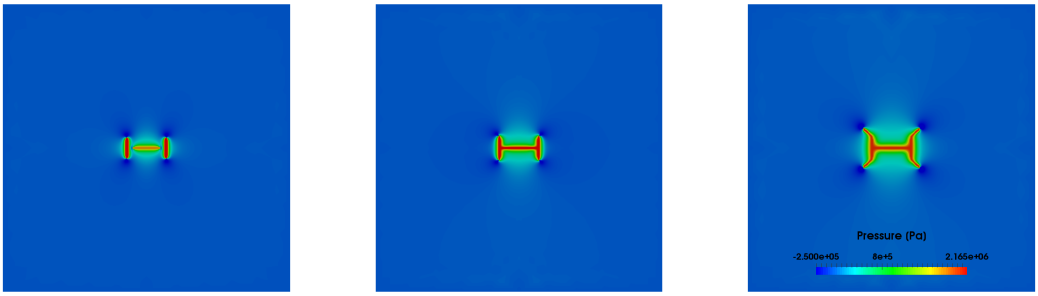

(a) t = 2 s **(b)** t = 3 s **(c)** t = 5 s

Fig. 20: Fluid driven propagation and coalescence of fractures in homogeneous porosity field. $v_{\text{inject}} = 0.00025$ m/s. Fluid pressure at t = 2 s, 3 s, 5 s.

Due to the enhanced permeability along the crack, the pore pressure inside the crack is of similar magnitude. However, the boundary layer of the pore pressure plume grows in time and eventually coalesces at 5s.

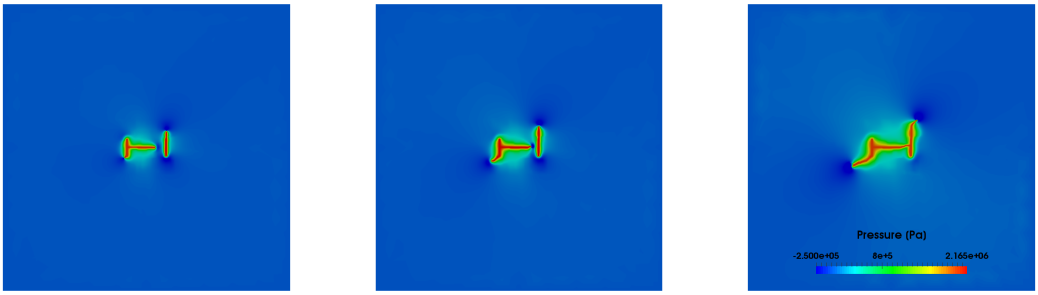

(a) t = 2 s **(b)** t = 3 s **(c)** t = 5 s

Fig. 21: Fluid driven propagation and coalescence of fractures in heterogeneous porosity field. $v_{\text{inject}} = 0.00025$ m/s. Fluid pressure at t = 2 s, 3 s, 5 s.

4.3.2 Influence of injection rate

Next we study the influence of the fluid injection rate on fracture patterns. v_{inject} is raised by ten times to 0.0025 m/s for an additional simulation on the heterogeneous porosity field. To compare the results, the pore pressure field at t = 0.2 s, 0.3 s and 0.5 s are presented in Fig. 22, so that the amount of fluid

injected into the domain are kept identical to those at t = 2 s, 3 s and 5 s of the low-injection-rate case. In the analytical framework introduced by Adachi and Detournay [2008], the change of injection may affect the values of the dimensionless toughness coefficient $\mathcal{K} \propto (\frac{1}{Q_0})^{\frac{1}{4}}$ and the leak-off coefficient $\mathcal{C} \propto (\frac{t}{Q_0^3})^{\frac{1}{6}}$, where Q_0 being the injection flux rate [Adachi and Detournay, 2008]. In particular the increase of the prescribed Darcy velocity v_{inject} may lead to lower $\mathcal{K}$, which means that a lower ratio of energy rate is expended in fracturing compared to the fluid viscous dissipation, and also a lower value of $\mathcal{C}$, which indicates that the fracture propagation takes longer time to transit from no-leak-off to leak-off dominated regime. These predictions from the analytical model is consistent with our numerical results shown in Figs. 21 and 22. In the high-injection-rate case, the increased injection velocity results in sharper pore pressure gradient across the crack and the surrounding host matrix. The pressure concentration zone becomes thinner and leak off is less profound compared to the low-injection-rate counterpart shown in Fig. 21. The increased injection rate does not only lead to a more storage-dominated behavior, but also alters the crack pattern. As shown in Fig. 22, the higher injection rate allows more excess pore pressure build up and the negative pore pressure near the tip of the cracks are also more significant. Through the hydro-mechanical coupling effect, this leads to a slightly different crack patterns compared with Fig. 21.

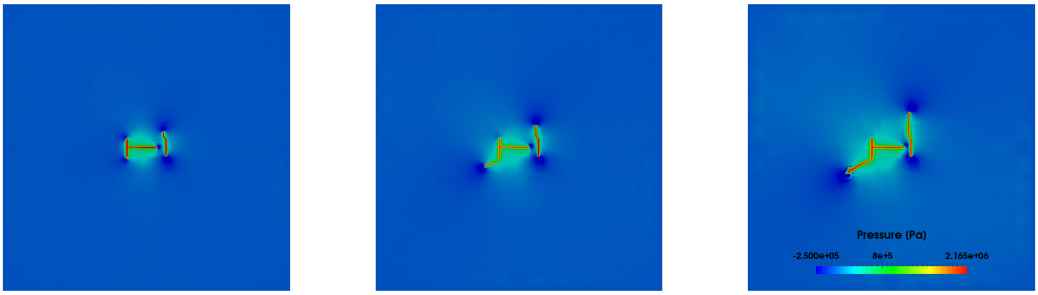

(a) t = 0.2 s **(b)** t = 0.3 s **(c)** t = 0.5 s

Fig. 22: Fluid driven propagation and coalescence of fractures in heterogeneous porosity field. $v_{\text{inject}} = 0.0025$ m/s. Fluid pressure at t = 0.2 s, 0.3 s, 0.5 s.

4.3.3 Interaction of compaction bands and fractures

Since a portion of the injected fluid will be stored inside the cracks when the permeability is low, it will expand the fracture and compress the surrounding porous matrix. For material with low G_{CB}, this could lead to the formation of compaction band in the vicinity of the fracture. This is consistent with the results of the simulations performed on a heterogeneous porosity field with $G_{CB} = 0.1\, kJ/m^2$ at reference porosity $\phi_0 = 0.2$ (Fig. 23). Before propagation of the embedded fractures, anti-crack nucleates in the vicinity of one tip of the horizontal crack that lies in high porosity area. It propagates rapidly towards the other tip of the horizontal crack following a curved path. The path represents the region where maximum compressive strain takes place. Anti-crack branching and coalescence is observed in Fig. 23.

The onset of anti-crack could be postponed as the material G_{CB} is increased. $G_{CB} = 2\, kJ/m^2$ at reference porosity ϕ_0 is adopted in the new simulation and Fig. 24 illustrates the compaction band evolution. The compaction band (anti-crack) this time appears after the coalescence of the left and center fractures. It is formed underneath the joint compression of these two expanding cracks. Again the compaction band exhibits branching, with one branch extending rapidly towards the other tip of the center crack, and the other branch connecting the tip of the left crack. Notice that in this work we assume the compaction band is formed in a brittle manner. Hence, the compaction band formed almost spontaneously following the peak loading. As a result, the crack patterns shown in Figs. 23 and 24 are formed within one single time step in which the nonlocal eigen-erosion scheme is used to search for a new equilibrium in this particular case.

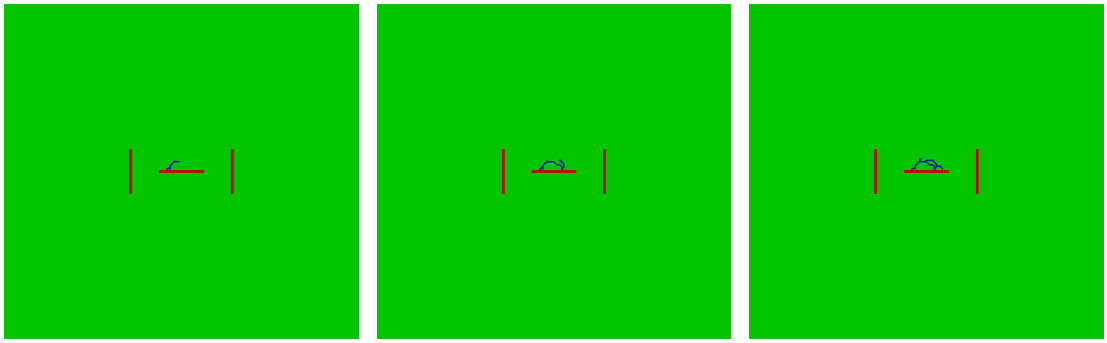

(a) Iteration 10 **(b)** Iteration 30 **(c)** Iteration 50

Fig. 23: Onset and propagation of compaction band near pressurized fractures in heterogeneous porosity field. $G_{CB} = 0.1\ kJ/m^2$ at reference porosity $\phi_0 = 0.2$. $v_{\text{inject}} = 0.00025$ m/s. Compaction band starts to form and propagate at time t = 0.2 s. The configurations at 10th, 30th, 50th iteration of anti-crack tracking algorithm at time t = 1.8 s are presented to illustrate the evolution of compaction band path. Red: crack set; Blue: compaction band set.

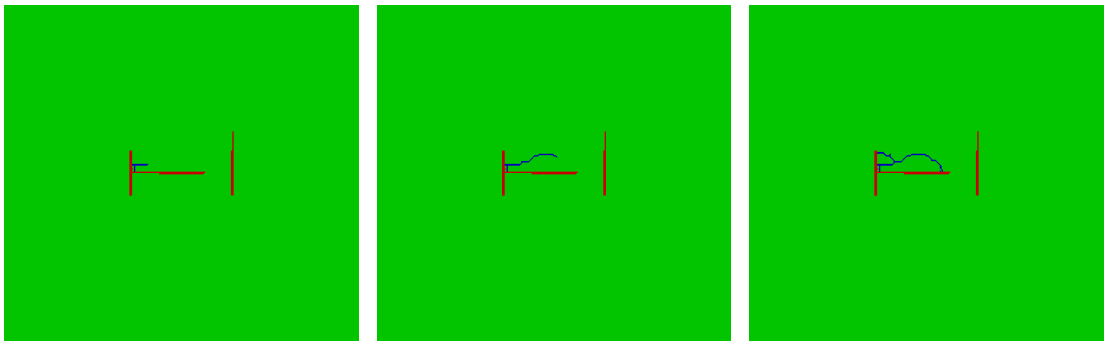

(a) Iteration 10 **(b)** Iteration 30 **(c)** Iteration 50

Fig. 24: Onset and propagation of compaction band near pressurized fractures in heterogeneous porosity field. $G_{CB} = 2\ kJ/m^2$ at reference porosity $\phi_0 = 0.2$. $v_{\text{inject}} = 0.00025$ m/s. Compaction band starts to form and propagate at time t = 1.8 s. The configurations at 10th, 30th, 50th iteration of anti-crack tracking algorithm at time t = 1.8 s are presented to illustrate the evolution of compaction band path. Red: crack set; Blue: compaction band set.

Altogether this series of simulations of fluid-driven fracture coalescence demonstrate the capability and potential of the unified eigen-erosion model in predicting complex crack and anti-crack patterns in large-scale geomechanics and geoenvironmental problems.

5 Conclusion

As point out in Holcomb et al. [2007], the existing computational model has not yet progressed to the point to analyze the influence of fluid flow on the formation and propagation of compaction band. Nor is it clear how does the compaction band and cracks interact in various drainage conditions. This work is intended to fill these knowledge gaps with important implications for petroleum engineering, reservoir management and geological disposals of nuclear waste and carbon dioxide storage. By introducing a unified Griffith-type variational framework capable of simulating the onset, propagation and coalescence of both fracture and compaction bands as Griffith-type flaws in *fluid-infiltrating* porous media. This is achieved

without (1) requiring any prior knowledge on the fracture and compaction band patterns and (2) introducing any nodal variables such as phase field. By associating the eigen-deformation modes of fracture and compaction bands with the corresponding fracture and compaction band energy functionals, the interplay between the fracture and compaction band are captured in the numerical examples. In addition, we have introduced a nonlocal algorithm to capture the evolving anisotropic effective permeability and circumvent the mesh dependence demonstrated commonly in the element erosion approach. Consequently, the numerical model exhibits the similar advantages of variational fracture and phase-field fracture model, without introducing any additional degree of freedoms to represent fractures and compaction bands. This simplicity greatly reduces the complexity of the solver and allows one to implement the fracture and compaction band models as nonlocal constitutive laws coupled with the classical field equations for poromechanics. Our numerical examples also demonstrate that the proposed model has good rate of convergence, even without any adaptive mesh refinement.

6 Acknowledgments

This research is supported by the Earth Materials and Processes program at the US Army Research Office under grant contract W911NF-14-1-0658, W911NF-15-1-0442 and W911NF-15-1-0581, Sandia National Laboratories under grant contract 1557089 as well as the Mechanics of Material program at National Science Foundation under grant contract CMMI-1462760. These supports are gratefully acknowledged. The authors are also grateful for receiving the support of Dresden Junior Fellowship from Technische Universität Dresden during their visit to Dresden where a portion of this paper is written. The authors also thank Professor John W Rudnicki and Professor Teng-fong Wong for fruitful discussion on the anti-crack model and the porosity reduction of compaction band.

7 Appendix: Finite element formulation of the hydraulic fracture in saturated porous media

One of the major advantages of the proposed approach is that there is no need to change the field equation, as well as the corresponding weak, Galerkin and matrix form of the hydro-mechanics model. The introduction of regularized element erosion can be regarded simply as non-local solid and hydraulic constitutive laws employed in standard mixed finite element formulation for poromechanics problem. As a result, the formulation of the stabilized finite element model used in this paper is only included here for completeness. Readers interested at the details of theory and implementation of the u/p formulation may refer to Sun et al. [2013, 2014], Sun [2015], Wang and Sun [2016a,b].

To construct the macroscopic hydro-mechanical boundary-value problem, consider a porous media domain $\mathcal{B}$ with its boundary $\partial\mathcal{B}$ composed of Dirichlet boundaries (solid displacement $\partial\mathcal{B}_{\boldsymbol{u}}$, pore pressure $\partial\mathcal{B}_p$) and Von Neumann boundaries (solid traction $\partial\mathcal{B}_{\boldsymbol{t}}$, fluid flux $\partial\mathcal{B}_q$) satisfying

$$\begin{cases} \partial\mathcal{B} = \overline{\partial\mathcal{B}_{\boldsymbol{u}} \cup \partial\mathcal{B}_{\boldsymbol{t}}} = \overline{\partial\mathcal{B}_p \cup \partial\mathcal{B}_q} \\ \emptyset = \partial\mathcal{B}_{\boldsymbol{u}} \cap \partial\mathcal{B}_{\boldsymbol{t}} = \partial\mathcal{B}_p \cap \partial\mathcal{B}_q \end{cases} \tag{29}$$

The prescribed boundary conditions are

$$\begin{cases} \boldsymbol{u} = \overline{\boldsymbol{u}} \text{ on } \partial\mathcal{B}_{\boldsymbol{u}} \\ \boldsymbol{\sigma}\cdot\boldsymbol{n} = \overline{\boldsymbol{t}} \text{ on } \partial\mathcal{B}_{\boldsymbol{t}} \\ p^f = \overline{p} \text{ on } \partial\mathcal{B}_p \\ -\boldsymbol{n}\cdot\boldsymbol{Q} = \overline{Q} \text{ on } \partial\mathcal{B}_{\boldsymbol{Q}} \end{cases} \tag{30}$$

where $\boldsymbol{n}$ is outward unit normal on surface $\partial\mathcal{B}$.

For model closure, the initial conditions are imposed as

$$p^f = p_0^f,\ \boldsymbol{u} = \boldsymbol{u_0} \text{ at } t = t_0 \tag{31}$$

Following the standard procedures of the variational formulation, the weak form of the balance of linear momentum, fluid mass in intact porous medium and fluid mass in fracture are:

$$\begin{aligned} G \;:\; & V_{\boldsymbol{u}} \times V_p \times V_\eta \to \mathbb{R} \\ G(\boldsymbol{u}, p^f, \boldsymbol{\eta}) = & \int_{\mathcal{B}} \nabla \boldsymbol{\eta} : (\boldsymbol{\sigma}' - B p^f \boldsymbol{I}) \, \mathrm{dV} - \int_{\partial \mathcal{B}_t} \boldsymbol{\eta} \cdot \bar{\boldsymbol{t}} \, \mathrm{d}\Gamma = 0 \end{aligned} \tag{32}$$

$$\begin{aligned} H \;:\; & V_{\boldsymbol{u}} \times V_p \times V_\psi \to \mathbb{R} \\ H(\boldsymbol{u}, p^f, \psi) = & \int_{\mathcal{B}} \psi B \nabla \cdot \dot{\boldsymbol{u}} \, \mathrm{dV} + \int_{\mathcal{B}} \psi \frac{1}{M} \dot{p^f} \, \mathrm{dV} \\ & - \int_{\mathcal{B}} \nabla \psi \cdot [\boldsymbol{k} \cdot (-\nabla p^f)] \, \mathrm{dV} \\ & - \int_{\partial B_Q} \psi \overline{\boldsymbol{Q}} \, \mathrm{d}\Gamma = 0 \end{aligned} \tag{33}$$

$$\begin{aligned} H' \;:\; & V_{\boldsymbol{u}} \times V_p \times V_\psi \to \mathbb{R} \\ H(\boldsymbol{u}, p^f, \psi) = & \int_{\mathcal{B}} \psi \nabla \cdot \dot{\boldsymbol{u}} \, \mathrm{dV} + \int_{\mathcal{B}} \psi \frac{1}{K_f} \dot{p^f} \, \mathrm{dV} \\ & - \int_{\mathcal{B}} \nabla \psi \cdot [\boldsymbol{k_f} \cdot (-\nabla p^f)] \, \mathrm{dV} \\ & - \int_{\partial B_Q} \psi \overline{\boldsymbol{Q}} \, \mathrm{d}\Gamma = 0 \end{aligned} \tag{34}$$

The displacement and pore pressure trial spaces for the weak form are defined as

$$V_{\boldsymbol{u}} = \{\boldsymbol{u} : \mathcal{B} \to \mathbb{R}^3 | \boldsymbol{u} \in [H^1(\mathcal{B})]^3, \boldsymbol{u}|_{\partial B_u} = \overline{\boldsymbol{u}}\} \tag{35}$$

$$V_p = \{p^f : \mathcal{B} \to \mathbb{R} | p^f \in H^1(\mathcal{B}), p^f|_{\partial B_p} = \overline{p}\} \tag{36}$$

and the corresponding admissible spaces of variations are defined as

$$V_{\boldsymbol{\eta}} = \{\boldsymbol{\eta} : \mathcal{B} \to \mathbb{R}^3 | \boldsymbol{\eta} \in [H^1(\mathcal{B})]^3, \boldsymbol{\eta}|_{\partial B_u} = \boldsymbol{0}\} \tag{37}$$

$$V_\psi = \{\psi : \mathcal{B} \to \mathbb{R} | \psi \in H^1(\mathcal{B}), \psi|_{\partial B_p} = 0\} \tag{38}$$

H^1 denotes the Sobolev space of degree one, which is the space of square integrable function whose weak derivative up to order 1 are also square integrable.

The spatially discretized equations can be derived following the standard Galerkin procedure. Shape functions $\boldsymbol{N_u}$ and $\boldsymbol{N_p}$ are used for approximation of solid motion $\boldsymbol{u}$, $\dot{\boldsymbol{u}}$ and pore pressure p^f, $\dot{p^f}$, respectively:

$$\begin{cases} \boldsymbol{u} = \boldsymbol{N_u} \bar{\boldsymbol{u}}, \;\; \dot{\boldsymbol{u}} = \boldsymbol{N_u} \dot{\bar{\boldsymbol{u}}}, \;\; \boldsymbol{\eta} = \boldsymbol{N_u} \bar{\boldsymbol{\eta}} \\ p^f = \boldsymbol{N_p} \bar{\boldsymbol{p}}^f, \;\; \dot{p^f} = \boldsymbol{N_p} \dot{\bar{\boldsymbol{p}}}^f, \;\; \psi = \boldsymbol{N_p} \bar{\boldsymbol{\psi}} \end{cases} \tag{39}$$

with $\bar{\boldsymbol{u}}$ being the nodal solid displacement vector, $\bar{\boldsymbol{p}}^f$ being the nodal pore pressure vector, $\dot{\bar{\boldsymbol{u}}}$, $\dot{\bar{\boldsymbol{p}}}^f$ being their time derivatives, and $\bar{\boldsymbol{\eta}}$, $\bar{\boldsymbol{\psi}}$ being their variations. The gradient of the shape functions are $\boldsymbol{B_u} = \frac{1}{2}(\nabla \boldsymbol{N_u} + \nabla \boldsymbol{N_u}^T)$ and $\boldsymbol{B_p} = \nabla \boldsymbol{N_p}$.

The adopted 2D four-node quadrilateral element interpolates the displacement and pore pressure field with the same order $\boldsymbol{N_u} = \boldsymbol{N_p}$. This combination does not inherently satisfy the inf-sup condition [White and Borja, 2008]. Therefore a stabilization procedure is necessary. In this study, the fluid pressure Laplacian scheme is applied. This scheme consists of adding the following stabilization term to the balance of fluid mass equation:

$$\int_{\mathcal{B}} \nabla \psi \, \alpha_{stab} \, \nabla \dot{p^f} \mathrm{dV} \tag{40}$$

with α_{stab} a scale factor depending on element size and material properties of the porous media [Truty and Zimmermann, 2006].

The semi-discretized finite element equations for balance of linear momentum and balance of fluid mass in intact porous medium are written as:

$$\begin{cases} G(\boldsymbol{u}, p^f, \boldsymbol{\eta}) = 0 \\ H(\boldsymbol{u}, p^f, \psi) = 0 \end{cases} \Longrightarrow \begin{cases} \boldsymbol{K^u}\bar{\boldsymbol{u}} - \boldsymbol{K^{up}}\bar{\boldsymbol{p}}^f = \boldsymbol{F^1_{ext}} \\ \boldsymbol{C_1}\dot{\bar{\boldsymbol{u}}} + (\boldsymbol{C_2} + \boldsymbol{C_{stab}})\dot{\bar{\boldsymbol{p}}}^f + \boldsymbol{K^p}\bar{\boldsymbol{p}}^f = \boldsymbol{F^2_{ext}} \end{cases} \tag{41}$$

The expressions for each matrices and vectors are as following, assuming linear elastic behavior of the solid skeleton with $\boldsymbol{D_e}$ being the material stiffness matrix:

$$\begin{cases} \boldsymbol{K^u} = \int_{\mathcal{B}} \boldsymbol{B_u}^{\mathrm{T}} \boldsymbol{D_e} \boldsymbol{B_u} \mathrm{dV} \\ \boldsymbol{K^{up}} = \int_{\mathcal{B}} B \boldsymbol{B_u}^{\mathrm{T}} \boldsymbol{m} \boldsymbol{N_p} \mathrm{dV} \\ \boldsymbol{C_1} = \int_{\mathcal{B}} B \boldsymbol{N_p}^{\mathrm{T}} \boldsymbol{m}^{\mathrm{T}} \boldsymbol{B_u} \mathrm{dV} \\ \boldsymbol{m} = [110]^T \text{in 2D} \\ \boldsymbol{C_2} = \int_{\mathcal{B}} \frac{1}{M} \boldsymbol{N_p}^{\mathrm{T}} \boldsymbol{N_p} \mathrm{dV} \\ \boldsymbol{C_{stab}} = \int_{\mathcal{B}} \boldsymbol{B_p}^{\mathrm{T}} \alpha_{stab} \boldsymbol{B_p} \mathrm{dV} \\ \boldsymbol{K^p} = \int_{\mathcal{B}} \boldsymbol{B_p}^{\mathrm{T}} \boldsymbol{k} \boldsymbol{B_p} \mathrm{dV} \\ \boldsymbol{F^1_{ext}} = \int_{\partial \mathcal{B}_t} \boldsymbol{N_u}^{\mathrm{T}} \bar{\boldsymbol{t}} \mathrm{d}\Gamma \\ \boldsymbol{F^2_{ext}} = \int_{\partial B_Q} \boldsymbol{N_p}^{\mathrm{T}} \overline{\boldsymbol{Q}} \mathrm{d}\Gamma \end{cases} \tag{42}$$

For elements representing the fracture in porous medium, the matrix equations are similar, with $B = 1$, $M = K_f$ and $\boldsymbol{k} = \boldsymbol{k}_f$.

The equation system (41) can be rewritten in a compact form:

$$\boldsymbol{M}\boldsymbol{v} + \boldsymbol{K}\boldsymbol{d} = \boldsymbol{F^{ext}} \tag{43}$$

where $\boldsymbol{M} = \begin{bmatrix} \boldsymbol{0} & \boldsymbol{0} \\ \boldsymbol{C_1} & (\boldsymbol{C_2} + \boldsymbol{C_{stab}}) \end{bmatrix}$, $\boldsymbol{v} = \begin{Bmatrix} \dot{\bar{\boldsymbol{u}}} \\ \dot{\bar{\boldsymbol{p}}}^f \end{Bmatrix}$, $\boldsymbol{K} = \begin{Bmatrix} \boldsymbol{K^u} & -\boldsymbol{K^{up}} \\ \boldsymbol{0} & \boldsymbol{K^p} \end{Bmatrix}$, $\boldsymbol{d} = \begin{Bmatrix} \bar{\boldsymbol{u}} \\ \bar{\boldsymbol{p}}^f \end{Bmatrix}$ and $\boldsymbol{F^{ext}} = \begin{Bmatrix} \boldsymbol{F^1_{ext}} \\ \boldsymbol{F^2_{ext}} \end{Bmatrix}$.

The transient equation is integrated implicitly in time using the predictor-corrector scheme based on the generalized trapezoidal rule. It consists of satisfying the equation (43) at time t_{n+1}:

$$\boldsymbol{M}\boldsymbol{v_{n+1}} + \boldsymbol{K}\boldsymbol{d_{n+1}} = \boldsymbol{F^{ext}_{n+1}} \tag{44}$$

with the solution

$$\boldsymbol{d_{n+1}} = \tilde{\boldsymbol{d}} + \alpha \Delta t \boldsymbol{v_{n+1}} \tag{45}$$

where the subscripts n and $n+1$ denote that the variables are evaluated at time t_n and t_{n+1}, respectively; Δt is the time step; α is the integration parameter. $\tilde{\boldsymbol{d}} = \boldsymbol{d_n} + (1-\alpha)\Delta t \boldsymbol{v_n}$ is referred to as the predicted solution. The corrector step consists of solving the $\boldsymbol{v_{n+1}}$ by:

$$(\boldsymbol{M} + \alpha \Delta t \boldsymbol{K})\boldsymbol{v_{n+1}} = \boldsymbol{F^{ext}_{n+1}} - \boldsymbol{K}\tilde{\boldsymbol{d}} \tag{46}$$

and compute the corrected $\boldsymbol{d_{n+1}}$ by (45).

References

José I Adachi and Emmanuel Detournay. Plane strain propagation of a hydraulic fracture in a permeable rock. *Engineering Fracture Mechanics*, 75(16):4666–4694, 2008.

Hanen Amor, Jean-Jacques Marigo, and Corrado Maurini. Regularized formulation of the variational brittle fracture with unilateral contact: numerical experiments. *Journal of the Mechanics and Physics of Solids*, 57(8):1209–1229, 2009.

Marco A Antonellini, Atilla Aydin, and David D Pollard. Microstructure of deformation bands in porous sandstones at arches national park, utah. *Journal of structural geology*, 16(7):941–959, 1994.

Francisco Armero and C Callari. An analysis of strong discontinuities in a saturated poro-plastic solid. *International journal for numerical methods in engineering*, 46(10):1673–1698, 1999.

Atilla Aydin, Ronaldo I Borja, and Peter Eichhubl. Geological and mathematical framework for failure modes in granular rock. *Journal of Structural Geology*, 28(1):83–98, 2006.

Jack W Baker, Andrew Seifried, Jose E Andrade, and Qiushi Chen. Characterization of random fields at multiple scales: an efficient conditional simulation procedure and applications in geomechanics. *Applications of Statistics and Probability in Civil Engineering*, page 347, 2011.

Patrick Baud, Emmanuelle Klein, and Teng-fong Wong. Compaction localization in porous sandstones: spatial evolution of damage and acoustic emission activity. *Journal of Structural Geology*, 26(4):603–624, 2004.

Jacob Bear. *Dynamics of fluids in porous media*. Elsevier Publishing Company, New York, 1972.

JA Begley and JD Landes. The j integral as a fracture criterion. In *Fracture Toughness: Part II*. ASTM International, 1972.

Pierre Bésuelle and John W Rudnicki. Localization: shear bands and compaction bands. *International Geophysics*, 89:219–321, 2003.

Maurice A Biot. General theory of three-dimensional consolidation. *Journal of applied physics*, 12(2):155–164, 1941.

TJ Boone, PA Wawrzynek, and AR Ingraffea. Simulation of the fracture process in rock with application to hydrofracturing. In *International Journal of Rock Mechanics and Mining Sciences & Geomechanics Abstracts*, volume 23, pages 255–265. Elsevier, 1986.

Michael J Borden, Clemens V Verhoosel, Michael A Scott, Thomas JR Hughes, and Chad M Landis. A phase-field description of dynamic brittle fracture. *Computer Methods in Applied Mechanics and Engineering*, 217:77–95, 2012.

Blaise Bourdin, Gilles A Francfort, and Jean-Jacques Marigo. The variational approach to fracture. *Journal of elasticity*, 91(1-3):5–148, 2008.

Benoit Carrier and Sylvie Granet. Numerical modeling of hydraulic fracture problem in permeable medium using cohesive zone model. *Engineering fracture mechanics*, 79:312–328, 2012.

Elli-Maria Charalampidou, Stephen A Hall, Sergei Stanchits, Gioacchino Viggiani, and Helen Lewis. Shear-enhanced compaction band identification at the laboratory scale using acoustic and full-field methods. *International Journal of Rock Mechanics and Mining Sciences*, 67:240–252, 2014.

Alexandre I Chemenda. Origin of compaction bands: Anti-cracking or constitutive instability? *Tectonophysics*, 499(1):156–164, 2011.

Z Chen, SP Narayan, Z Yang, and SS Rahman. An experimental investigation of hydraulic behaviour of fractures and joints in granitic rock. *International Journal of Rock Mechanics and Mining Sciences*, 37(7): 1061–1071, 2000.

Jinhyun Choo, Joshua A White, and Ronaldo I Borja. Hydromechanical modeling of unsaturated flow in double porosity media. *International Journal of Geomechanics*, page D4016002, 2016.

JD Clayton and J Knap. A geometrically nonlinear phase field theory of brittle fracture. *International Journal of Fracture*, 189(2):139–148, 2014.

JD Clayton and J Knap. Phase field modeling and simulation of coupled fracture and twinning in single crystals and polycrystals. *Computer Methods in Applied Mechanics and Engineering*, 2016.

René de Borst. Fluid flow in fractured and fracturing porous media: A unified view. *Mechanics Research Communications*, 2016.

René de Borst and Clemens V Verhoosel. Gradient damage vs phase-field approaches for fracture: Similarities and differences. *Computer Methods in Applied Mechanics and Engineering*, 2016.

Emmanuel Detournay. Mechanics of hydraulic fractures. *Annual Review of Fluid Mechanics*, 48:311–339, 2016.

David E Dunn, Lester J LaFountain, and Robert E Jackson. Porosity dependence and mechanism of brittle fracture in sandstones. *Journal of Geophysical Research*, 78(14):2403–2417, 1973.

John D Eshelby. The determination of the elastic field of an ellipsoidal inclusion, and related problems. In *Proceedings of the Royal Society of London A: Mathematical, Physical and Engineering Sciences*, volume 241, pages 376–396. The Royal Society, 1957.

Patrick E Farrell and Corrado Maurini. Linear and nonlinear solvers for variational phase-field models of brittle fracture. *International Journal for Numerical Methods in Engineering*, 2016.

Haakon Fossen, Richard A Schultz, and Anita Torabi. Conditions and implications for compaction band formation in the navajo sandstone, utah. *Journal of Structural Geology*, 33(10):1477–1490, 2011.

Craig D Foster and Talisa Mohammad Nejad. Embedded discontinuity finite element modeling of fluid flow in fractured porous media. *Acta Geotechnica*, 8(1):49–57, 2013.

G. A. Francfort and J. J. Marigo. Revisiting brittle fracture as an energy minimization problem. *Journal of the Mechanics and Physics of Solids*, 46(8):1319–1342, 1998.

P Gupta and CA Duarte. Simulation of non-planar three-dimensional hydraulic fracture propagation. *International Journal for Numerical and Analytical Methods in Geomechanics*, 38(13):1397–1430, 2014.

B Haimson. Micromechanisms of borehole instability leading to breakouts in rocks. *International Journal of Rock Mechanics and Mining Sciences*, 44(2):157–173, 2007.

B Haimson and H Lee. Borehole breakouts and compaction bands in two high-porosity sandstones. *International Journal of Rock Mechanics and Mining Sciences*, 41(2):287–301, 2004.

BC Haimson. Fracture-like borehole breakouts in high-porosity sandstone: Are they caused by compaction bands? *Physics and Chemistry of the Earth, Part A: Solid Earth and Geodesy*, 26(1):15–20, 2001.

BC Haimson and I Song. Laboratory study of borehole breakouts in cordova cream: a case of shear failure mechanism. In *International journal of rock mechanics and mining sciences & geomechanics abstracts*, volume 30, pages 1047–1056. Elsevier, 1993.

Bezalel Haimson, Charles Fairhurst, et al. Initiation and extension of hydraulic fractures in rocks. *Society of Petroleum Engineers Journal*, 7(03):310–318, 1967.

David Holcomb, John W Rudnicki, Kathleen A Issen, and Kurt Sternlof. Compaction localization in the earth and the laboratory: state of the research and research directions. *Acta Geotechnica*, 2(1):1–15, 2007.

DJ Holcomb and WA Olsson. Compaction localization and fluid flow. *Journal of Geophysical Research: Solid Earth*, 108(B6), 2003.

KA Issen and JW Rudnicki. Theory of compaction bands in porous rock. *Physics and Chemistry of the Earth, Part A: Solid Earth and Geodesy*, 26(1):95–100, 2001.

R Katsman and E Aharonov. A study of compaction bands originating from cracks, notches, and compacted defects. *Journal of Structural Geology*, 28(3):508–518, 2006.

R Katsman, E Aharonov, and H Scher. Numerical simulation of compaction bands in high-porosity sedimentary rock. *Mechanics of materials*, 37(1):143–162, 2005.

R Katsman, E Aharonov, and BC Haimson. Compaction bands induced by borehole drilling. *Acta Geotechnica*, 4(3):151–162, 2009.

Amir R Khoei. *Extended finite element method: theory and applications*. John Wiley & Sons, 2014.

AR Khoei, M Vahab, E Haghighat, and S Moallemi. A mesh-independent finite element formulation for modeling crack growth in saturated porous media based on an enriched-fem technique. *International Journal of Fracture*, 188(1):79–108, 2014.

H Lee, T Moon, and BC Haimson. Borehole breakouts induced in arkosic sandstones and a discrete element analysis. *Rock Mechanics and Rock Engineering*, 49(4):1369–1388, 2016a.

M Lee and B Haimson. Laboratory study of borehole breakouts in lac du bonnet granite: a case of extensile failure mechanism. In *International journal of rock mechanics and mining sciences & geomechanics abstracts*, volume 30, pages 1039–1045. Elsevier, 1993.

Myung W Lee. *Proposed moduli of dry rock and their application to predicting elastic velocities of sandstones*. US Department of the Interior, US Geological Survey, 2005.

Sanghyun Lee, Mary F Wheeler, and Thomas Wick. Pressure and fluid-driven fracture propagation in porous media using an adaptive finite element phase field model. *Computer Methods in Applied Mechanics and Engineering*, 305:111–132, 2016b.

ER Leeman et al. Absolute rock stress measurements using a borehole trepanning stress-relieving technique. In *The 6th US Symposium on Rock Mechanics (USRMS)*. American Rock Mechanics Association, 1964.

Christian Linder and F Armero. Finite elements with embedded branching. *Finite Elements in Analysis and Design*, 45(4):280–293, 2009.

Chun Liu, David D Pollard, Shang Deng, and Atilla Aydin. Mechanism of formation of wiggly compaction bands in porous sandstone: 1. observations and conceptual model. *Journal of Geophysical Research: Solid Earth*, 120(12):8138–8152, 2015.

Christian Miehe and Steffen Mauthe. Phase field modeling of fracture in multi-physics problems. part iii. crack driving forces in hydro-poro-elasticity and hydraulic fracturing of fluid-saturated porous media. *Computer Methods in Applied Mechanics and Engineering*, 304:619–655, 2016.

Christian Miehe, Martina Hofacker, and Fabian Welschinger. A phase field model for rate-independent crack propagation: Robust algorithmic implementation based on operator splits. *Computer Methods in Applied Mechanics and Engineering*, 199(45):2765–2778, 2010.

Stephanie J Mitchell, Anna Pandolfi, and Michael Ortiz. Effect of brittle fracture in a metaconcrete slab under shock loading. *Journal of Engineering Mechanics*, 142(4):04016010, 2016.

PN Mollema and MA Antonellini. Compaction bands: a structural analog for anti-mode i cracks in aeolian sandstone. *Tectonophysics*, 267(1):209–228, 1996.

SeonHong Na and WaiChing Sun. Wave propagation and strain localization in a fully saturated softening porous medium under the non-isothermal conditions. *International Journal for Numerical and Analytical Methods in Geomechanics*, pages n/a–n/a, 2016. ISSN 1096-9853. doi: 10.1002/nag.2505. URL http://dx.doi.org/10.1002/nag.2505.

Mohamed Buhary Nooru-Mohamed. *Mixed-mode fracture of concrete: an experimental approach*. TU Delft, Delft University of Technology, 1992.

Amos Nur and JD Byerlee. An exact effective stress law for elastic deformation of rock with fluids. *Journal of Geophysical Research*, 76(26):6414–6419, 1971.

Anna Pandolfi and Michael Ortiz. An eigenerosion approach to brittle fracture. *International Journal for Numerical Methods in Engineering*, 92(8):694–714, 2012.

Steven R Pride and James G Berryman. Linear dynamics of double-porosity dual-permeability materials. i. governing equations and acoustic attenuation. *Physical Review E*, 68(3):036603, 2003.

Laura J Pyrak-Nolte, Larry R Myer, Neville GW Cook, Paul A Witherspoon, et al. Hydraulic and mechanical properties of natural fractures in low permeability rock. In *6th ISRM Congress*. International Society for Rock Mechanics, 1987.

Carl E Renshaw. On the relationship between mechanical and hydraulic apertures in rough-walled fractures. *Journal of Geophysical Research: Solid Earth*, 100(B12):24629–24636, 1995.

John W Rudnicki. *Eshelby's technique for analyzing inhomogeneities in geomechanics*. Springer, 2011.

JW Rudnicki. Models for compaction band propagation. *Geological Society, London, Special Publications*, 284 (1):107–125, 2007.

JW Rudnicki and KR Sternlof. Energy release model of compaction band propagation. *Geophysical Research Letters*, 32(16), 2005.

Saeed Salimzadeh and Nasser Khalili. A three-phase xfem model for hydraulic fracturing with cohesive crack propagation. *Computers and Geotechnics*, 69:82–92, 2015.

Bernd Schmidt, Fernando Fraternali, and Michael Ortiz. Eigenfracture: an eigendeformation approach to variational fracture. *Multiscale Modeling & Simulation*, 7(3):1237–1266, 2009.

Richard A Schultz, Chris H Okubo, and Haakon Fossen. Porosity and grain size controls on compaction band formation in jurassic navajo sandstone. *Geophysical Research Letters*, 37(22), 2010.

S Secchi and BA Schrefler. A method for 3-d hydraulic fracturing simulation. *International journal of fracture*, 178(1-2):245–258, 2012.

Sergei Stanchits, Jerome Fortin, Yves Gueguen, and George Dresen. Initiation and propagation of compaction bands in dry and wet bentheim sandstone. In *Rock Physics and Natural Hazards*, pages 846–868. Springer, 2009.

Kurt R Sternlof, John W Rudnicki, and David D Pollard. Anticrack inclusion model for compaction bands in sandstone. *Journal of Geophysical Research: Solid Earth*, 110(B11), 2005.

W. Sun, J.T. Ostien, and A.G. Salinger. A stabilized assumed deformation gradient finite element formulation for strongly coupled poromechanical simulations at finite strain. *International Journal for Numerical and Analytical Methods in Geomechanics*, 37(16):2755–2788, 2013.

W. Sun, Q. Chen, and J.T. Ostien. Modeling hydro-mechanical responses of strip and circular footings on saturated collapsible geomaterials. *Acta Geotechnica*, 2014. doi: 10.1007/s11440-013-0276-x.

WaiChing Sun. A unified method to predict diffuse and localized instabilities in sands. *Geomechanics and Geoengineering*, 8(2):65–75, 2013.

WaiChing Sun. A stabilized finite element formulation for monolithic thermo-hydro-mechanical simulations at finite strain. *International Journal for Numerical Methods in Engineering*, 103(11):798–839, 2015. doi: 10.1002/nme.4910.

WaiChing Sun, Jose E Andrade, and John W Rudnicki. Multiscale method for characterization of porous microstructures and their impact on macroscopic effective permeability. *International Journal for Numerical Methods in Engineering*, 88(12):1260–1279, 2011a.

WaiChing Sun, José E Andrade, John W Rudnicki, and Peter Eichhubl. Connecting microstructural attributes and permeability from 3d tomographic images of in situ shear-enhanced compaction bands using multiscale computations. *Geophysical Research Letters*, 38(10), 2011b.

von K Terzaghi. The shearing resistance of saturated soils and the angle between the planes of shear. In *Proceedings of the 1st International Conference on Soil Mechanics and Foundation Engineering*, volume 1, pages 54–56. Harvard University Press Cambridge, MA, 1936.

Andrzej Truty and Thomas Zimmermann. Stabilized mixed finite element formulations for materially nonlinear partially saturated two-phase media. *Computer methods in applied mechanics and engineering*, 195(13):1517–1546, 2006.

Veronika Vajdova and Teng-Fong Wong. Incremental propagation of discrete compaction bands: Acoustic emission and microstructural observations on circumferentially notched samples of bentheim. *Geophysical Research Letters*, 30(14), 2003.

Baoshan Wang, Yong Chen, and Teng-fong Wong. A discrete element model for the development of compaction localization in granular rock. *Journal of Geophysical Research: Solid Earth*, 113(B3), 2008.

JSY Wang and D Elsworth. Permeability changes induced by excavation in fractured tuff. In *Proceedings of the 37th US Rock Mechanics Symposium, Rock Mechanics for Industry*, volume 2, pages 751–757, 1999.

Kun Wang and WaiChing Sun. A semi-implicit discrete-continuum coupling method for porous media based on the effective stress principle at finite strain. *Computer Methods in Applied Mechanics and Engineering*, 304:546 – 583, 2016a. ISSN 0045-7825.

Kun Wang and Waiching Sun. A semi-implicit micropolar discrete-to-continuum method for granular materials. In M Papadrakakis, V Papadopoulos, G Stefanou, and V Plevris, editors, *Proceedings of European Congress on Computational Methods in Applied Science and Engineering*, number June, pages 5–10, Crete Island, 2016b.

MF Wheeler, T Wick, and W Wollner. An augmented-lagrangian method for the phase-field approach for pressurized fractures. *Computer Methods in Applied Mechanics and Engineering*, 271:69–85, 2014.

Joshua A White and Ronaldo I Borja. Stabilized low-order finite elements for coupled solid-deformation/fluid-diffusion and their application to fault zone transients. *Computer Methods in Applied Mechanics and Engineering*, 197(49):4353–4366, 2008.

Paul Adams Witherspoon, Joseph SY Wang, K Iwai, and John E Gale. Validity of cubic law for fluid flow in a deformable rock fracture. *Water resources research*, 16(6):1016–1024, 1980.

Ziqiong Zheng, John Kemeny, and Neville GW Cook. Analysis of borehole breakouts. *Journal of Geophysical Research: Solid Earth*, 94(B6):7171–7182, 1989.

Robert W Zimmerman and In-Wook Yeo. Fluid flow in rock fractures: From the navier-stokes equations to the cubic law. *Dynamics of fluids in fractured rock*, pages 213–224, 2000.

Mark D Zoback, Daniel Moos, Larry Mastin, and Roger N Anderson. Well bore breakouts and in situ stress. *Journal of Geophysical Research: Solid Earth*, 90(B7):5523–5530, 1985.

MD Zoback, F Rummel, R Jung, and CB Raleigh. Laboratory hydraulic fracturing experiments in intact and pre-fractured rock. In *International Journal of Rock Mechanics and Mining Sciences & Geomechanics Abstracts*, volume 14, pages 49–58. Elsevier, 1977.